

CHAPTER 3

# Thermohaline Structure and Water Masses in the Bering Sea

**Vladimir A. Luchin, Vladimir A. Menovshchikov, and  
Vladimir M. Lavrentiev**

*Far Eastern Regional Hydrometeorological Research Institute (FERHI),  
Vladivostok, Russia*

**Ronald K. Reed**

*Pacific Marine Environmental Laboratory, Seattle, Washington*

## Abstract

Data from 35,700 hydrographic stations were grouped in areas of 1° latitude and 2° longitude and monthly, seasonal, and annual means calculated. We examined temperature, salinity, and water masses of the Bering Sea, studying their vertical structure, temporal variability, and features of their spatial and temporal distribution. We also considered data from coastal observations, information on the meteorological regime, and river outflow.

## Previous Investigations

The first summaries of hydrographic research in the Bering Sea date from the previous century (Tanner 1890, Rathburn 1894). They contained general information about the temperature and salinity of the water. From 1906 to 1929, deepwater hydrographic work was not conducted; it was renewed only in the 1930s. Observations obtained during these years served as the basis for the work of Ratmanov (1937), who gave the first presentation of the distribution of temperature and salinity in the sea and the origins of the Anadyr and Olyutorsk cold zones. He also noted the interaction of waters from the northern part of the Pacific Ocean and the Bering Sea.

The shallow-water regime of the northern and eastern parts of the sea were studied by Goodman et al. (1942). They used data from expeditions in 1937 and 1938. Leonov (1947, 1960) extended the research in the Bering Sea to the start of the 1950s. He distinguished four water masses in the sea: the upper Bering Sea, intermediate Bering Sea, deep Pacific Ocean,

and polar. He also studied the water balance, thermal regime, and distribution of salinity and density in the sea.

From 1950 to 1953, the Institute of Oceanology of the USSR carried out a set of studies in the Bering Sea; the studies continued in 1955 and 1956 in conjunction with the Pacific Ocean Institute of Fisheries Ecology and Oceanography (TINRO). Data from these studies formed the basis of work by Burkov (1958), Dobrovolskiy et al. (1959), Ivanenkov (1964), and Arsenev (1967). Summarizing observations from 1932 to 1955, Dobrovolskiy and Arsenev (1961) examined the influence of morphological and climatic factors on processes in the sea, described the vertical structure and origins of water masses, and summarized the distribution of parameters in different seasons. They distinguished three types of vertical water structure (arctic, subarctic, and temperate latitudes) and also examined in detail seasonal variability of temperature in the top 200-300 m layer. Ivanenkov (1964) also proposed a classification of water masses in the Bering Sea. In the deep basin, he distinguished four water masses: the surface Bering Sea, the subsurface, the intermediate, and the deep North Pacific. In the shallow water, he differentiated seven regions using the distribution of temperature, salinity, and chemical properties. In 1958, the Institute of Oceanology and TINRO began work on various expeditions. During three years, a total of 1,000 stations were occupied during the summer and winter. The results of this research are contained in the work of Natarov (1963). He concluded that the deep Bering Sea had the character of subarctic water, characterized by the presence in summer of four water masses: the warm surface layer from 0 to 50 m, the cold subsurface layer from 50 to 150-200 m, the warm intermediate layer from 200 to 600-800 m, and the deep water. In winter, this structure consisted of only three layers. Arsenev (1967) carried out a more complete study of the water masses of the Bering Sea. He used data from 1894 to 1959 and the results of earlier summaries. The author gave detailed characteristics of the main water masses and examined the factors causing their formation.

In recent years, Russian scientists have concentrated on the western part of the Bering Sea (Davydov and Lipetskiy 1970; Lazo 1971; Davydov 1972, 1984; Naumov and Khistyayev 1972). These authors noted the large role of the Kamchatka Current in the formation of the thermohaline regime of the shelf water near the east coast of Kamchatka. The distributions of chemical parameters also attest to the formation of eddies in Karagin and Olyutorsk bays (Davydov and Lipetskiy 1970; Davydov 1972, 1984).

An article by Poluektov and Khistyayev (1981) stands out from the more fragmentary work published in the 1970s and 1980s (Lazo 1971, Tiguntsev 1971, Naumov and Khistyayev 1972, Milyeiko 1973, Izrael' 1983, Yarichin 1984, Khen and Voronin 1986). Poluektov and Khistyayev systematized data of bathythermograph observations from 1971 to 1976 (more than 1,200 observations, taken from January to May). They studied the variation of the lower limit of the isothermal layer, distinguished types of tempera-

ture profiles, divided the area into five homogeneous regions, and calculated correlation coefficients between temperature at the surface and temperature in the lower layers.

Short-period variability of water temperature in Bering Strait was examined by Tiguntsev (1971). He found that water temperature varied by up to 6°C during the course of a day; this variation was a significant part of the total variability of temperature in this region. Khen and Voronin (1986) examined the influence of atmospheric processes and sea ice on the interannual oscillations of parameters in the eastern part of the Bering Sea. These authors distinguished three periods of warming and two periods of cooling in the shelf waters.

In the post-war years, Japanese organizations began to carry out expeditions in the Bering Sea. Most of the data were obtained from the ships *Oshoro Maru* and *Hokkusei Maru*. The results of these expeditions are reflected in the work of Mishima and Nishizawa (1955), Koto and Fuji (1958), Maeda et al. (1968), Kihara and Uda (1969), Kitano (1970), Ohtani (1969, 1973), and Takenouti and Ohtani (1974). Researchers examined the characteristics of the cold intermediate layer (Koto and Fuji 1958), the distribution of bottom temperature on the shelf, the penetration of warm water from the deep basin onto the shelf (Koto and Maeda 1965), and the distribution of temperature and salinity in the bottom layer of the shallow eastern part of the sea (Maeda et al. 1968). Maeda et al. (1968) also examined interannual variability of temperature and salinity in the bottom water on the shelf, showed the location of a cold zone southwest of St. Lawrence Island, and described the spreading of cold bottom water to the southeast, toward Bristol Bay. Kihara and Uda (1969) examined the formation of the bottom water mass in the eastern Bering Sea. They inferred that the sources were Alaskan coastal water, water from the northern part of the sea, and water from the Alaskan Stream.

Ohtani (1969, 1973) carried out the most complete summary of research conducted by Japanese and American expeditions from 1959 to 1966. He presented a detailed classification of the waters of the Bering Sea. He differentiated three water systems: oceanic, shelf, and continental. Ohtani noted links between systems of currents and the thermohaline structure of the water. He also gave a detailed characterization of shelf waters and examined the process of convective mixing in winter and the vertical distributions of temperature and salinity in the deep basin and on the shelf. More recently, work by Japanese researchers has dealt mainly with the eastern and southeastern regions of the sea. Results in various publications (Takenouti 1976, Kitani and Kawasaki 1979, Otake et al. 1983) examined the structure and conditions for the formation of subarctic water, as well as features of the fine structure of water near the continental slope.

Early American work in the Bering Sea was by Barnes and Thompson (1938) and Saur et al. (1952). In the 1950s and 1960s, American and Canadian scientists carried out programs to study the northern part of the

Pacific, including the Bering Sea. Observations from expeditions of this period were used in monographs and summaries (Dodimead et al. 1963; Favorite et al. 1961, 1976; Favorite 1974). Dodimead et al. (1963) also examined the oceanographic conditions in Bristol Bay. They noted the existence of an inner front dividing nearshore and mid-shelf waters. They also indicated the existence of an analogous front along the outer edge of the shelf.

Until about 1975, most of the American and Japanese research dealt with the deep part of the sea and the region of Bering Strait. Work in this period was done to determine the mean conditions in the sea (Hood and Kelley 1974), the structure of currents (Dowling 1962, Hughes et al. 1974), and to characterize water masses. Sayles et al. (1979) compiled an atlas of oceanographic characteristics and examined the water masses of the deep basin as well as the distribution of temperature, salinity, and dynamic topography of the water in individual seasons. A paper by Swift and Aagaard (1976) examined upwelling and mixing near Samalga Pass. They confirmed the existence of upwelling, which could occur along the entire length of the Aleutian Islands.

Coachman et al. (1975) were the first to summarize information obtained by American and Japanese expeditions in the region of Bering Strait from 1922 to 1973. Research distinguished three water masses there (Anadyr, Bering Shelf, and Alaskan Coastal). The authors made the important conclusion that lateral mixing is extremely limited in Bering Strait.

After 1975, American scientists concentrated on the study of the continental shelf. Their interest shifted from the study of climatic variability to processes at smaller scales. Research included the region from the Beaufort Sea to the Gulf of Alaska. Observations were reflected in works by Muench (1976), Coachman and Charnell (1977), Kinder (1977), Kinder and Coachman (1978), Reed (1978), Coachman (1979), Schumacher et al. (1979), Coachman et al. (1980), and Ingraham (1981). These significantly expanded knowledge about processes at various time scales on the shelf of the Bering Sea.

In 1981, Hood and Calder edited a monograph containing preliminary results of OCSEAP (Outer Continental Shelf Environmental Assessment Program) on the eastern shelf. Results of this program (Ingraham 1981, Kinder and Schumacher 1981, Muench et al. 1981, Mofjeld 1986) covered in detail the structure of the water, the meteorological and sea ice regimes, and the dynamics of the water. Kinder and Schumacher (1981) analyzed the structure of shelf waters. They summarized previous research, and examined data observed during 1975-1978. They divided the shelf into three structural zones (coastal, middle, and outer). The borders of their zones roughly conform to the 50 m and 100 m isobaths. The authors noted that the different regions are more pronounced in the summer.

Coachman (1986) summarized the physical research of the PROBES (Processes and Resources of the Bering Sea Shelf) program. He arrived at the conclusion that the water mass of the southeast part of the shelf could be regarded as a system with three regimes of physical processes, separated by fronts. He stressed the importance of the vertical distribution of water properties. In the frontal zones, important changes are observed in the balance of factors influencing features of the water masses. He also examined the most important physical processes that determine the formation of water masses.

## **Materials and Methods**

The data used are from deep-sea observations, carried out in the Bering Sea from 1932 to 1989. We processed data from 35,700 stations obtained during 588 cruises of three countries. Most of the data was collected by the U.S.S.R. (30,998 stations), but there is also material from Japanese (1,976 stations) and U.S. ships (2,726 stations). We examined short-period variability in temperature and salinity with data from 11 open-sea stations occupied many times from 1950 to 1989. All of the deep-ocean observations were subject to quality control. First, using analogous work (Belkin 1984, Gubenko and Tsipis 1984, Pereskokov 1984), we ascertained if our values were within the bounds of others' data. Then the data were divided by month. At standard depths, we calculated the mean and standard deviation of specific variables. Values greater than three standard deviations from the mean were rejected. Data were binned into trapezoids ( $1^\circ$  of latitude by  $2^\circ$  of longitude). In each trapezoid, we calculated the mean, maximum, minimum, and standard deviation of each variable at standard depths. The statistics were assigned to the center of their respective trapezoids. The distribution of oceanographic stations in the region is presented in Fig. 1. It is obvious that few studies occupied the center of the deep part of the sea. In the deep basin, the number of observations decreases sharply with depth. The number of 500 m stations in individual quadrants sometimes reaches  $\sim 200$ , while the number of stations in each quadrant having data at 1,000 m is less than 100. In all of the quadrants, there were fewer than 25 stations at 2,000 m and deeper.

Of the total data, 59% are from the summer months (June–September). In the present work, we consider the active layer to be the upper layer of water, in which we observe an annual signal in the physical parameters. To determine its lower limit, we used profiles of the vertical distribution of monthly mean characteristics. To calculate the lower limit of the upper quasi-homogeneous layer, we took the point of intersection of the two tangents to the profile of vertical distribution (to the surface quasi-homogeneous layer and in the layer of seasonal gradients). To differentiate water

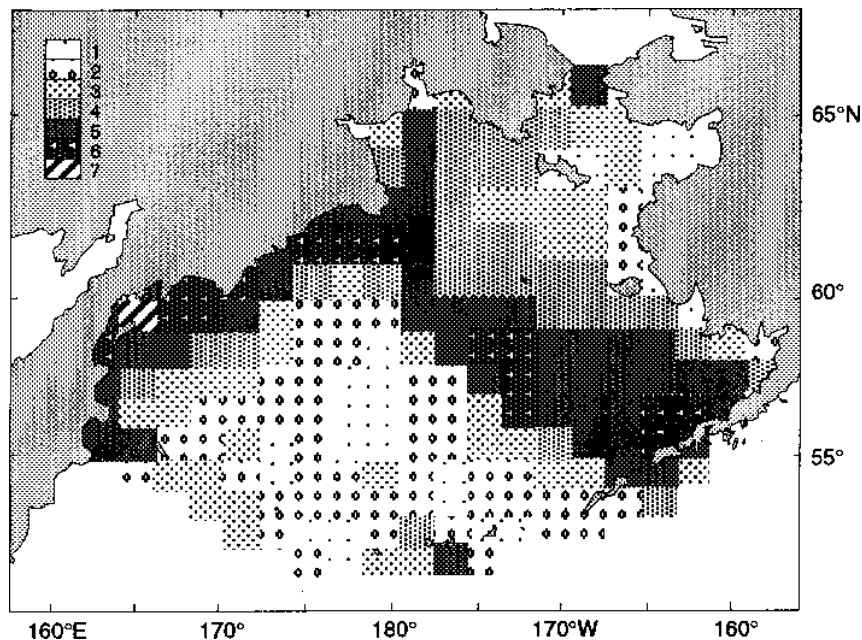


Figure 1. Distribution of oceanographic stations in the Bering Sea: (1) 0-25 stations, (2) 26-50, (3) 51-100, (4) 101-200, (5) 201-500, (6) 501-1,000, and (7) more than 1,001 stations.

mass parameters, we used the method of temperature-salinity (TS) analysis.

## Temperature

### *Vertical Distribution*

The Bering Sea is located in the region of subarctic water structure, whose main feature is the presence of cold and warm intermediate layers (Burkov 1958, Arsenev 1967, Filyushkin 1968, Moiseev 1978). The subarctic structure is most marked in the deep western basin. Profiles of the vertical distribution of temperature indicate that the Bering Sea water column may be divided into several layers. The active layer of the sea is most susceptible to thermodynamic effects from the air-sea interface. The topography of its depth is shown in Fig. 2a. In the eastern part of the sea, the depth of the active layer is generally less than 150 m. In the western half of the sea, it increases to as much as 250 m, except near the coast (Fig. 2a). Its vertical extent depends on the intensity of the exchanges at the air-sea interface and on features in the large-scale circulation. An additional factor

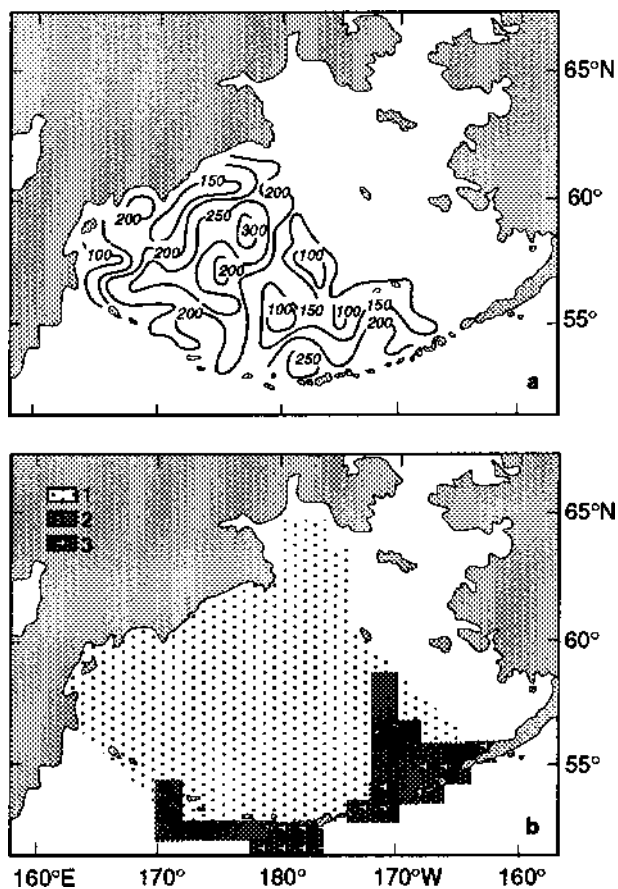


Figure 2. (a) Depth (m) of the lower boundary of the active layer; (b) A measure of the development of the cold intermediate layer: (1) well-developed, (2) weakly developed, and (3) not apparent.

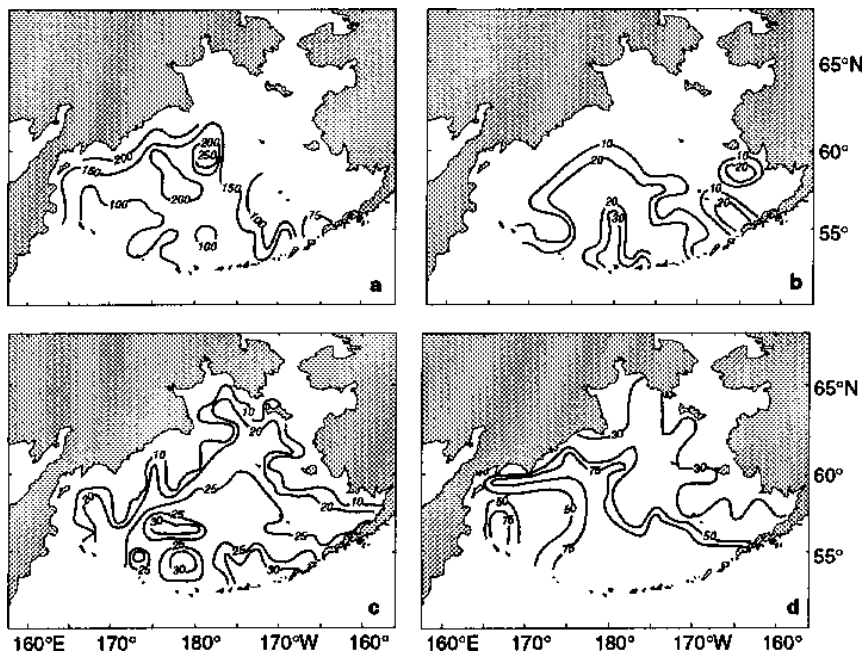


Figure 3. Depth of the lower boundary of the upper quasi-homogeneous layer: (a) January-March, (b) June-July, (c) August-September, and (d) November.

in determining its extent is the mixing of water in the passes of the Aleutian Islands.

The cold intermediate layer (CIL) is an important structural element of the active layer. It forms as a result of two processes: cooling of the water in autumn and winter and its warming in the spring and summer. Above and below the CIL, there are layers with increased temperature gradients. The CIL is not clearly obvious at some sites (Fig. 2b).

The vertical extent of the surface quasi-homogeneous layer (SQL) varies substantially during the course of the year and in different parts of the sea. Its maximum development is attained during the winter (Fig. 3a). In April and May, it is difficult to distinguish the SQL. During the warm period of the year, the minimum development of the SQL occurs with the greatest warming of the surface water in August-September (Fig. 3c). With the start of autumn (Fig. 3d), cooling of the water gradually increases the thickness of the SQL.

The formation of the CIL results from cooling of the sea in autumn and winter. Its vertical extent is limited to the depth attained by convection. Intensive cooling in winter leads to a homogeneous structure. The

characteristic CIL appears only when a surface-warmed layer is formed. The magnitude of the minimum temperature and the depth of its occurrence vary within fairly wide limits in the region. This is a consequence of the variations in the intensity of mixing processes in different parts of the Bering Sea, the effect of the "winterizing" of Pacific Ocean water, and features of its distribution in the Bering Sea. The temperature of the core of the CIL is a striking indication of advective processes occurring in the subsurface layers of the Bering Sea. The most intense inflow of heat occurs in the Aleutian passes east of 172°W.

The lowest temperatures in the core of the CIL (as low as  $-1.2^{\circ}\text{C}$ ) are seen on the shelf south and southwest of St. Lawrence Island. In July and August, the core temperature of the CIL increases. Because of the advection of Pacific Ocean water, the temperature at the core of the CIL near the Kamchatka Peninsula reaches  $1.8^{\circ}\text{--}2.4^{\circ}\text{C}$ . In September-October, wind speed increases, and thermal convection begins. The role of horizontal and vertical exchanges in the active layer of the sea increases. This leads to an increase in the magnitude of the core temperature of the CIL, especially on the shelf. At this time, the remaining cooled water exits the Bering Sea through Kamchatka Strait. The temperature and depth of the core of the warm intermediate layer (WIL) is determined by contact with the Pacific Ocean and by the extent of transformation of Pacific Ocean water in different parts of the sea. We can divide the deep part of the sea into two parts, separated by a line connecting Bering Island and St. Matthew Island. To the northwest of the line, the WIL is obvious, while to the southeast it is either absent or very weak. The core of the WIL is found at a depth of 250-500 m. Minimum values are seen in Near Strait and adjoining regions and in the southeastern part of the deep basin.

### ***High-Frequency Variability***

Large diurnal temperature fluctuations occur in areas where there is inflow of Pacific Ocean water into the sea (Fig. 4). In these regions, there are high current speeds, and the formation of eddies segregates waters with different characteristics. Maximum daily temperature variability (up to  $4^{\circ}\text{C}$ ) occurs at the shelf break and near coasts. In these regions, currents are intensified and there is also an increase in the probability of eddy formation. In gulfs and bays, there may be periodic replacement of low-salinity surface waters with water from the open sea or underlying depths. On the eastern shelf, however, diurnal temperature fluctuations do not exceed  $\sim 0.7^{\circ}\text{C}$ . In this region there are relatively small horizontal gradients of characteristics.

In winter, daily surface temperature fluctuations do not generally exceed  $0.2^{\circ}\text{C}$ . Below  $\sim 100$  m, however, a layer with significant gradients in characteristics forms. This leads to well-developed internal waves at this depth and to short-period variations in water temperature. Temperature variability observed in the 150-200 m layer (Fig. 4a) is primarily from tidal

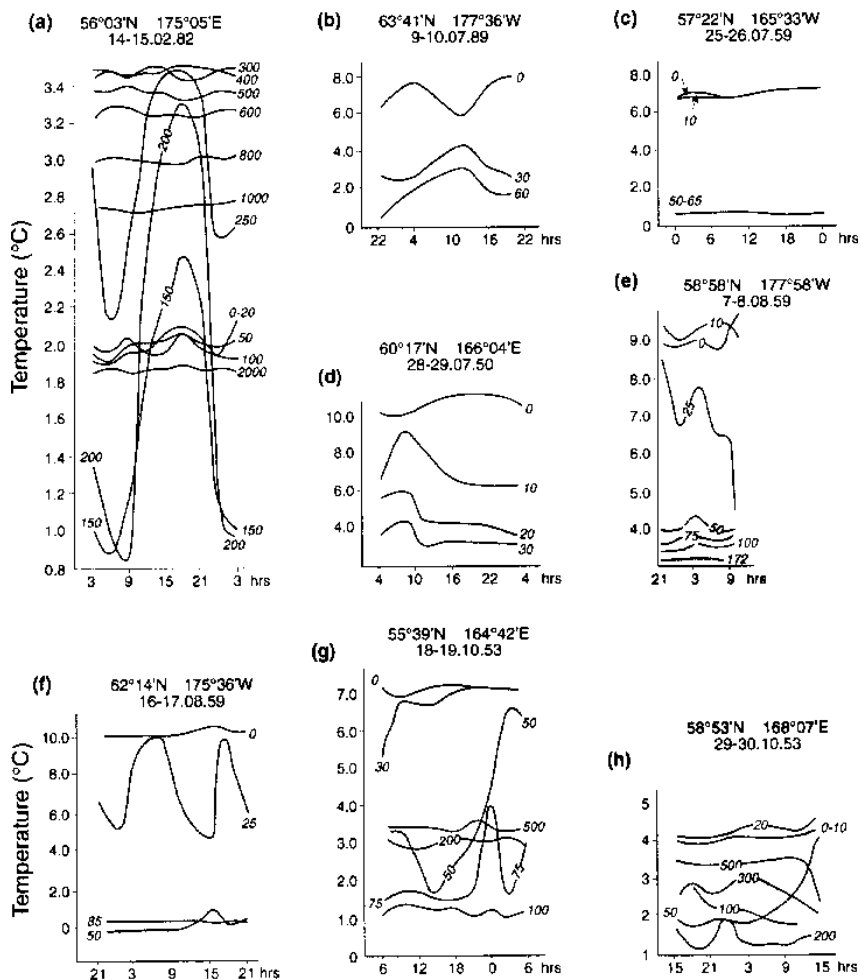


Figure 4. Daily variations of temperature at different times in various regions of the Bering Sea at different depths (m).

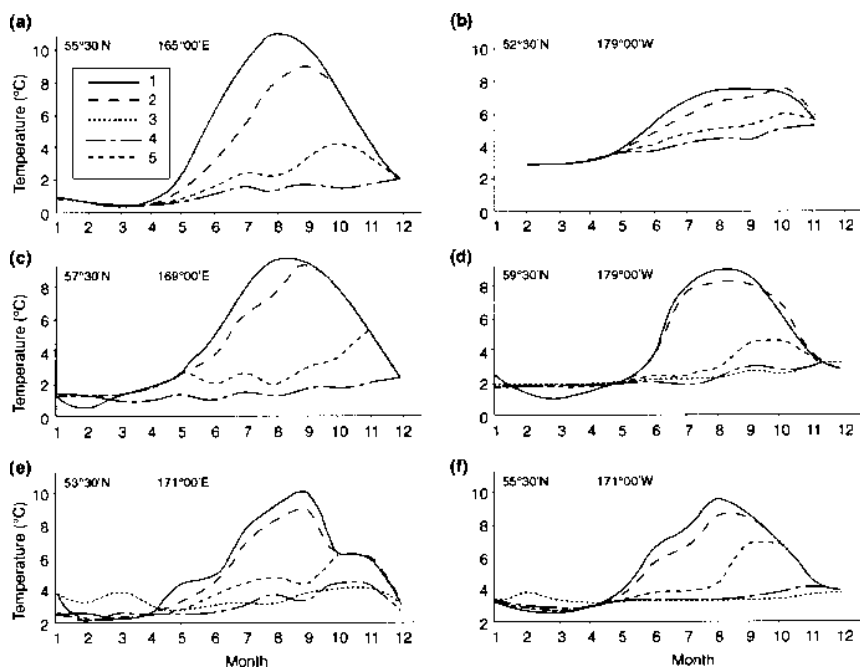


Figure 5. Intra-annual variability of water temperature in the Bering Sea at a depth of: (1) at the surface, (2) 20 m, (3) 50 m, (4) 100 m, and (5) 150 m, at the locations indicated.

effects, with some fortnightly variations being apparent. The range of daily temperature variation here is 1.0°-2.5°C.

In summer, subsurface layers may also have large temperature gradients and variations (Fig. 4). Temperatures may change by 2.0°-4.5°C during the day. In regions of the sea where dynamic processes are insignificant, temperature variability is minimum (Fig. 4c). At some stations, we observe the upwelling of underlying water to near the surface (Fig. 4e). In Pacific Ocean waters, two layers with high values of daily variability may form (Fig. 4g,h).

### Seasonal Variability

Seasonal temperature variability depends on the variability of the components of the heat balance at the sea surface and the redistribution of heat in deeper layers due to horizontal and vertical movement of water. In most of the Bering Sea, the maximum temperature of the surface water occurs in August. In areas such as Near Strait and the central Aleutian passes, the maximum may be displaced respectively to September and

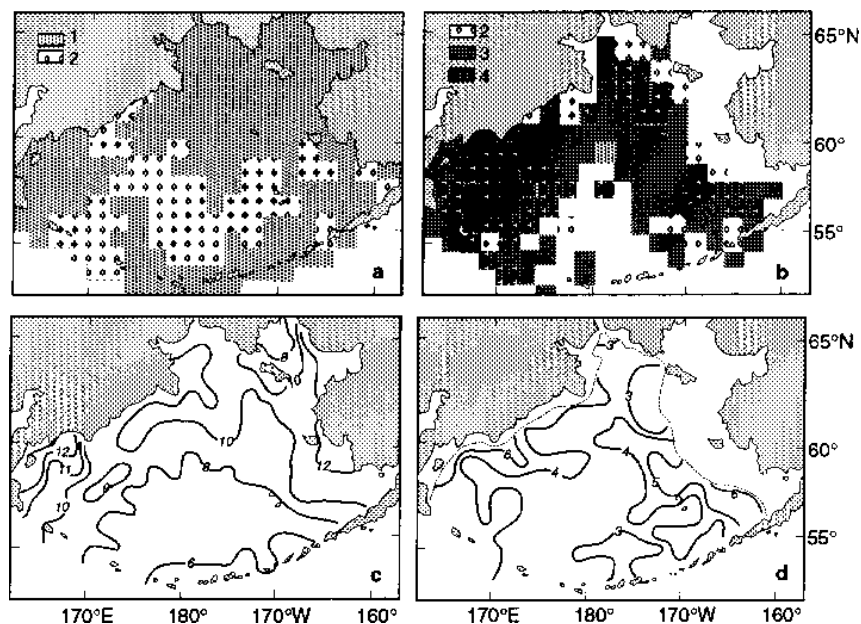


Figure 6. Timing of the occurrence of the maximum temperature: (a) at the surface, and (b) at 50 m: (1) August, (2) September, (3) October, and (4) November. Also, variation of temperature (degrees C) (c) at the surface, and (d) at 50 m.

August-October. In regions in the vicinity of the straits, the maximum temperature occurs in August-September (Figs. 5, 6a). Maximum temperatures at a depth of 20 m occur, as a rule, with the onset of thermal convection in September. In zones with intense vertical mixing, this shifts to August-September (Fig. 6). With increased depth in the water column, there is a further shift in the timing of the arrival of the maximum temperature. This is connected to processes of thermal convection and the intensity of horizontal and vertical exchange in the water column. The temperature at 50 m reaches its maximum value in October-November. In dynamically active regions, the peak temperature occurs earlier (Fig. 6b).

The minimum surface temperatures in the deep part of the Bering Sea occur in March-April. In areas of intense vertical mixing, they occur in April. Seasonal variability in surface temperature is shown in Figure 6c. Maximum magnitudes coincide with coastal regions of the sea, while the lowest values are observed in and near the Aleutian passes.

Seasonal temperature variability at 50 m is a factor of 2-4 less than at the sea surface (Fig. 6c,d). The greatest variability is seen in the gulfs and along the shelf break. Minimum temperature variability occurs in the straits

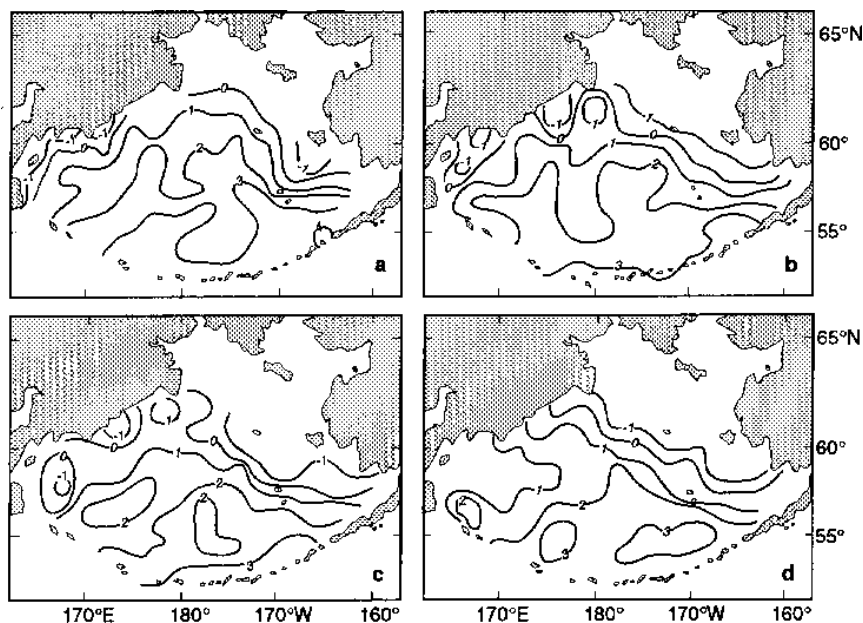


Figure 7. Distribution of the sea surface temperature ( $^{\circ}\text{C}$ ) of the Bering Sea: (a) January, (b) February, (c) March, and (d) April.

of the Aleutian Islands, in the central part of the eastern Bering Sea shelf, and in the Gulf of Anadyr.

At a depth of 100-150 m, seasonal temperature variability is generally  $<3^{\circ}\text{C}$  (Fig. 5). Maximum variations are seen in places where there is Pacific Ocean inflow, and also in regions of intense autumn-winter convection.

### ***Spatial and Temporal Distribution of Temperature***

In the Bering Sea, the year can be divided into two periods based on large-scale features of the distribution of sea surface temperature (Figs. 7-9). From November to June (winter type of distribution; Figs. 7-9), the Pacific Ocean water arriving in the Bering Sea is warmer than the Bering Sea water. This has two causes: first, Pacific Ocean water has a higher heat supply in its active layer, and second, vertical mixing in the Aleutian passes leads to a transfer of heat from underlying layers to the surface. In the warm part of the year (July-September; Figs. 8-9), water temperature near the Aleutian passes is significantly lower than in the Bering Sea. This is caused by the vertical mixing occurring in the passes. The temperature field in October is transitional between these two thermal conditions in the Bering Sea. The thermal regime in the Bering Sea depends to a large

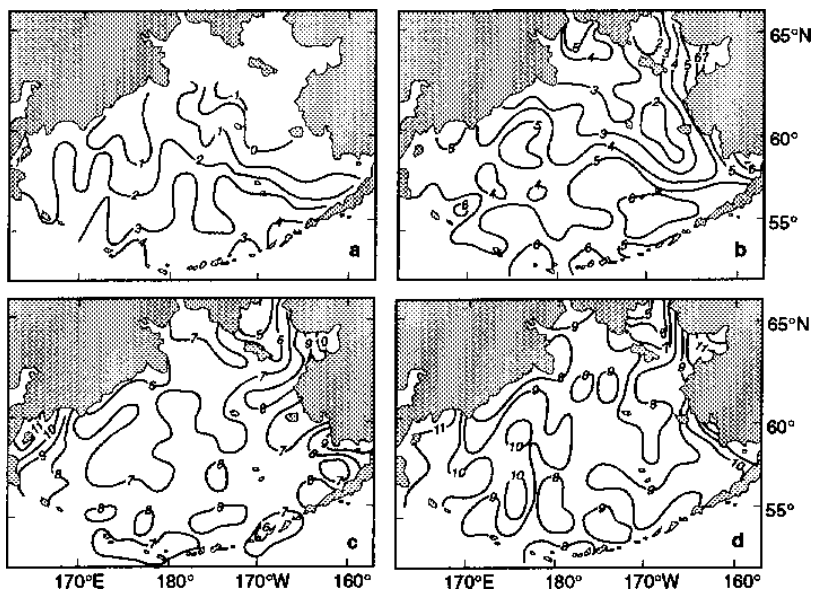


Figure 8. Distribution of the sea surface temperature ( $^{\circ}\text{C}$ ) of the Bering Sea: (a) May, (b) June, (c) July, and (d) August

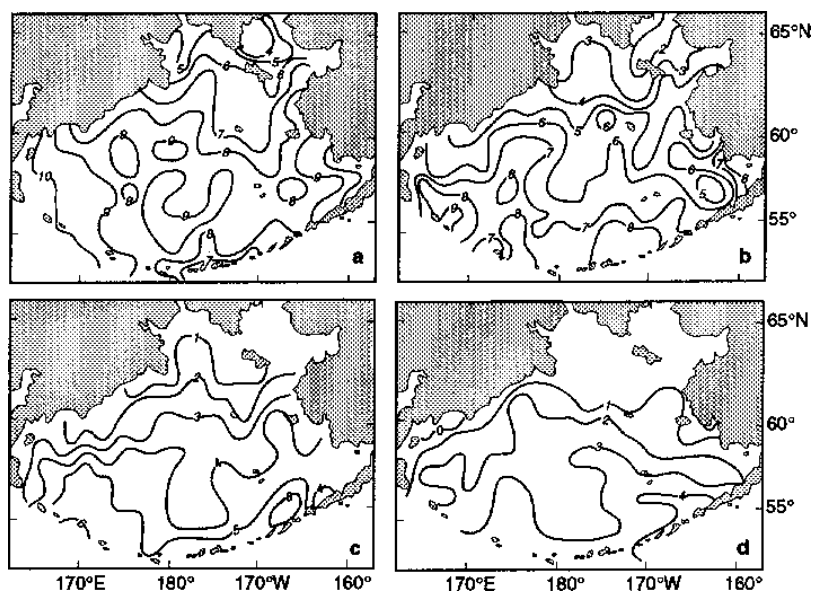


Figure 9. Distribution of the sea surface temperature ( $^{\circ}\text{C}$ ) of the Bering Sea: (a) September, (b) October, (c) November, and (d) December.

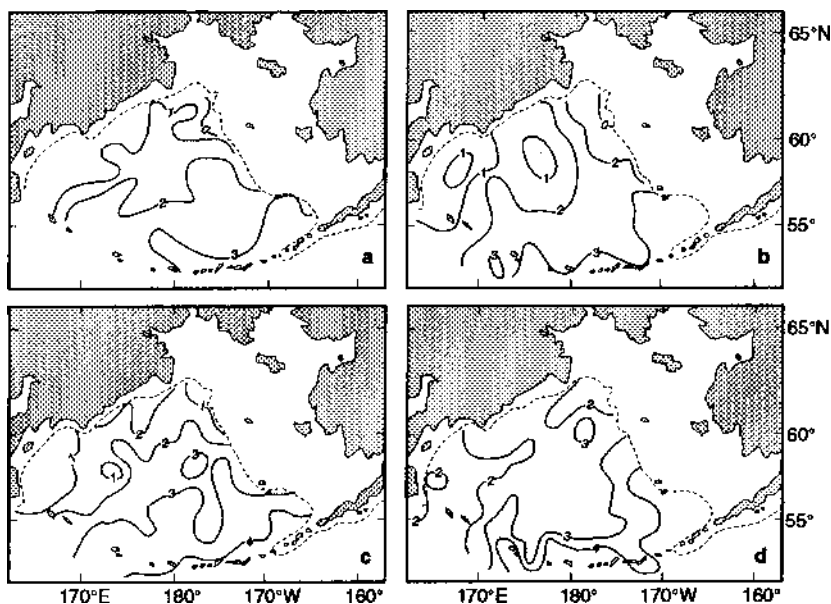


Figure 10. Distribution of the temperature ( $^{\circ}\text{C}$ ) of the Bering Sea at 100 m in: (a) March, (b) May, (c) August, and (d) October.

extent on water exchange with the Pacific Ocean and on further spreading of Pacific Ocean water within the Bering Sea. The configuration of the  $2^{\circ}\text{C}$  and  $3^{\circ}\text{C}$  isotherms in Figure 7 can illustrate the roles of different Aleutian passes in the exchange of water with the Pacific Ocean. From January to June (Figs. 7a,b, 8a,b), there is a hydrographic front between the shelf waters and the waters of the Bering Sea's deep basin. In December (Fig. 9d), two regions of inflow of warm Pacific Ocean water are seen: east of  $167^{\circ}\text{W}$ , and through the passes between  $171^{\circ}$  and  $178^{\circ}\text{E}$ .

Seasonal temperature variations at 100 m (Fig. 10) are small. Maximum temperatures ( $3^{\circ}\text{--}5^{\circ}\text{C}$ ) are noted in the eastern Aleutian Island passes. A general warming of temperatures from May to October is a consequence of the displacement of cold water from winter convection by warmer Pacific Ocean water.

At a depth of 200 m (Fig. 11), there are still appreciable horizontal gradients. This results from the main inflow of Pacific Ocean water occurring through Near Strait and the central Aleutian passes. Maximum temperature at this depth is in autumn (Fig. 11d). At this time, convective processes begin to be seen, as well as an increase in vertical and lateral water exchange linked to an increase in wind speed.

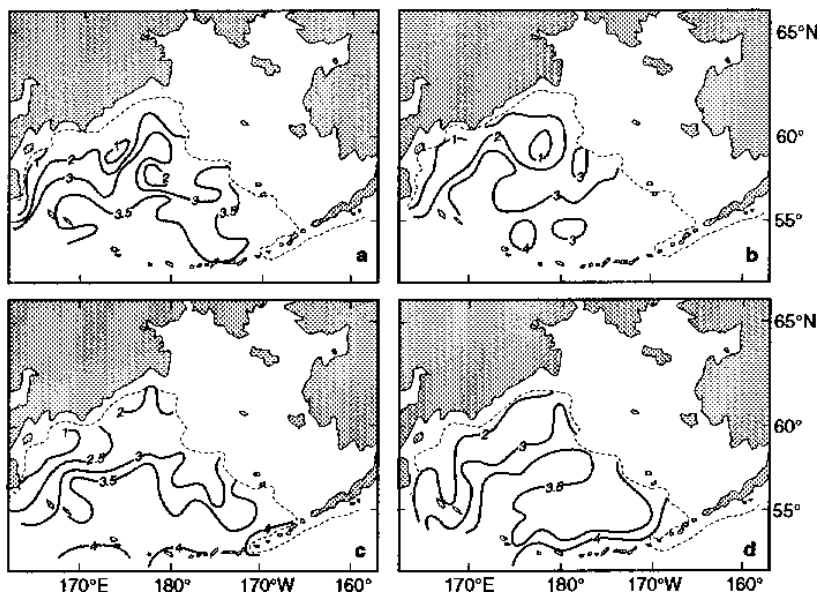


Figure 11. Distribution of the temperature ( $^{\circ}\text{C}$ ) of the Bering Sea at 200 m in: (a) March, (b) May, (c) August, and (d) October.

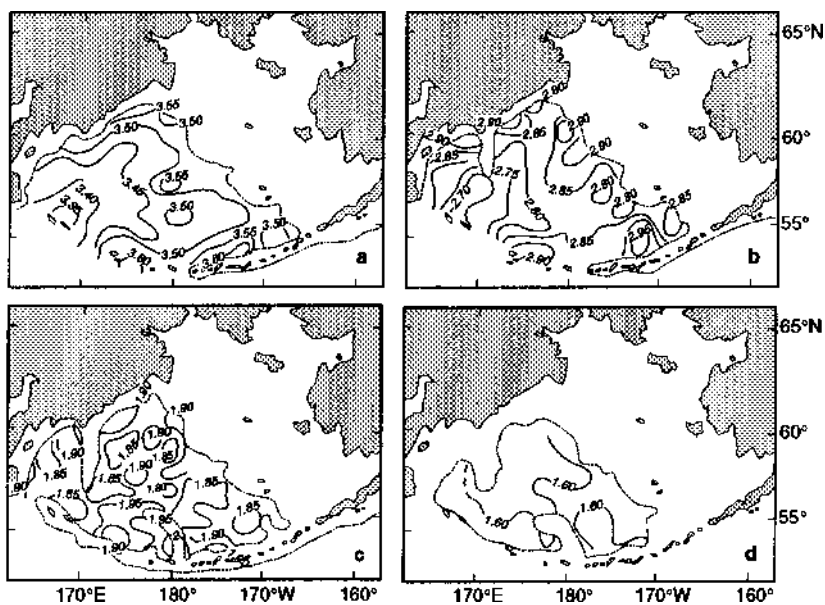


Figure 12. Temperature ( $^{\circ}\text{C}$ ) at a depth of: (a) 500 m, (b) 1,000 m, (c) 2,000 m, and (d) 3,000 m.

It is difficult to discern seasonal variability at depths greater than 200 m. At depths of 500 m and 1,000 m (Fig. 12), the main inflow of Pacific Ocean water occurs between the Commander Islands and 173°E. Temporal variations at these depths are less than 0.3°C. An increase in temperature is noted near the continental slope and near the Aleutian Islands east of 174°E. This may be associated with increased vertical mixing and the transfer of heat from overlying layers of water (Fig. 12a,b). At a depth of 2,000 m (Fig. 12c), water temperatures in the Bering Sea vary between 1.8° and 1.95°C, and at 3,000 m (Fig. 12d) they vary from 1.56°C to 1.70°C.

## **Salinity**

### ***Vertical Distribution***

The salinity of the water in the upper layer of the Bering Sea depends on advection of Pacific Ocean water, the hydrological cycle between the surface layer and atmosphere, continental drainage, ice formation, and melting of ice. Currents and mixing of water only redistribute salt. At greater depths, the salinity depends on currents and water exchange with the Pacific Ocean. Salinity in the Bering Sea increases with depth; however, during the period of ice formation, there may be a slight salinity inversion in the surface layer.

The highest variability occurs in the upper layer of the sea, with the seasonal halocline being part of this layer. The layer of the main thermocline is limited at its lower level by the depth of the sharp change in vertical gradients. In this layer the salinity always increases with depth. The deepest structural feature extends from the lower limit of the main halocline to the bottom.

In the Bering Sea, seasonal variability in salinity does not penetrate beyond 150 m. Minimum thickness of the active layer is observed in the shelf regions of the sea, as well as near the shelf break. Maximum thicknesses of the active layer are seen in regions where there is inflow of Pacific Ocean water. Minimum values of the depth of the bottom of the main halocline are seen in Near Strait. In deep water, salinity increases slightly with depth. The magnitude of the salinity gradient in the layer of the main halocline is 3-5 times greater than in the underlying water column.

### ***Short-Period Variability***

The observed data show that daily salinity variability on the whole depends on dynamic processes. Oscillations up to 0.10 ppt are observed in regions far from shore on the eastern Bering Sea shelf. This value is typical for both the surface and underlying depths. One reason for the small salinity variability is probably the relatively weak currents. In regions affected by the Kamchatka Current and in zones of inflow of Pacific Ocean water (e.g., Near Strait), daily variability in salinity increases to 0.2-0.4

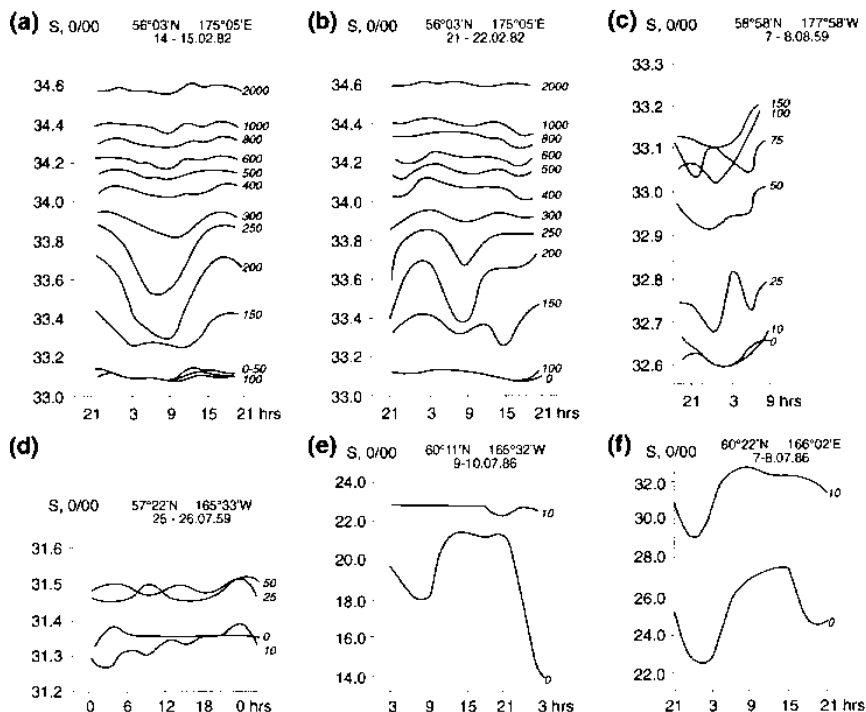


Figure 13. Hourly variations of salinity by date in various regions of the Bering Sea at different depths.

ppt. This increase is brought about by intense vertical and lateral exchange and by advection. In frontal zones, daily salinity variations increase to 1 ppt or more. Maximum values are observed in the surface layer.

During the cold part of the year, daily salinity variations in the upper layer practically disappear (Fig. 13). At the lower edge of the convective layer, however, salinity variability may reach 0.3-0.6 ppt (Fig. 13a). Temporal variation in salinity at the pycnocline indicates that the oscillations may be tidal. In the warm part of the year (Fig. 13c), two layers show increased magnitudes of daily variability: the lower boundary of the upper quasi-homogeneous layer and the layer affected by winter convection. In areas of the eastern Bering Sea shelf that are far from shore, daily salinity oscillations do not exceed ~0.2 ppt (Fig. 13c,d). Near the coast, the salinity oscillations strengthen, most notably in regions near the mouths of rivers (Fig. 13e,f). Greatest stability is seen in regions far from the coast. In zones where mixing of waters of different origin occurs, however, there is a substantial distortion of the vertical salinity distribution. In coastal

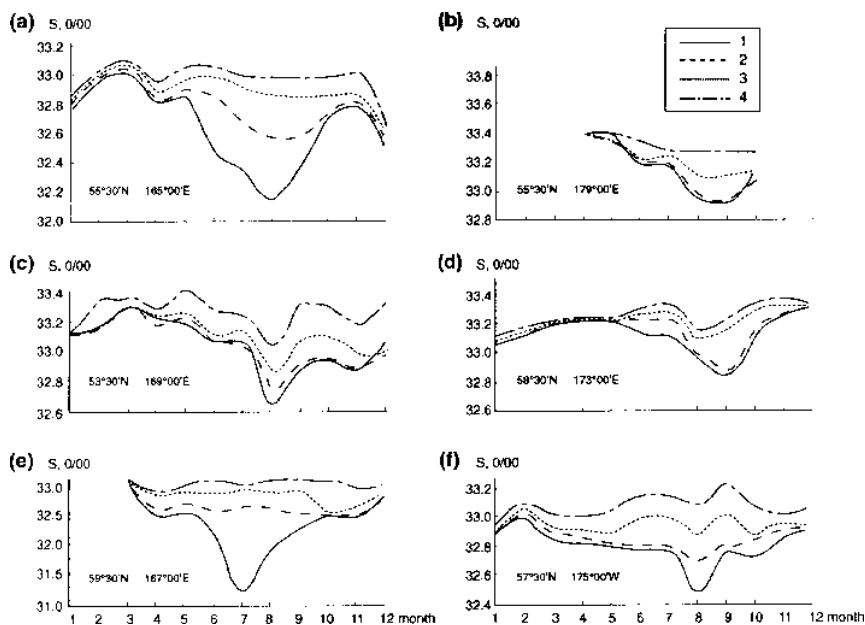


Figure 14. Intra-annual variability of salinity (ppt) in the Bering Sea at a depth of: (1) at the surface, (2) 20 m, (3) 50 m, and (4) 100 m.

and estuarine regions, major transformation of the vertical profile does not occur.

### Seasonal Variability

Seasonal variability in salinity is linked to oscillations in river outflow, the formation of ice cover, the balance between precipitation and evaporation from surface waters, and other factors. In the open part of the sea, annual salinity variation is substantially smaller than in nearshore areas. The highest variability in the deep sea occurs in the surface layer. Near shore, the density gradient between surface and subsurface waters increases, which impedes exchange between the two layers. Therefore the major salinity oscillations are limited to the upper 50 m (Fig. 14). Near the Aleutian Island passes and over the deep basin of the Bering Sea, the highest salinities in the active layer are often from March to May. Near the continental slope, the highest salinities occur in February-March. Minimum salinity in the deep part of the sea is often from July to September. Near the coast, salinity is minimum in July because of river flow. Over the deep basin in areas far from the coast, lowest salinities are often in August. Near the Aleutian

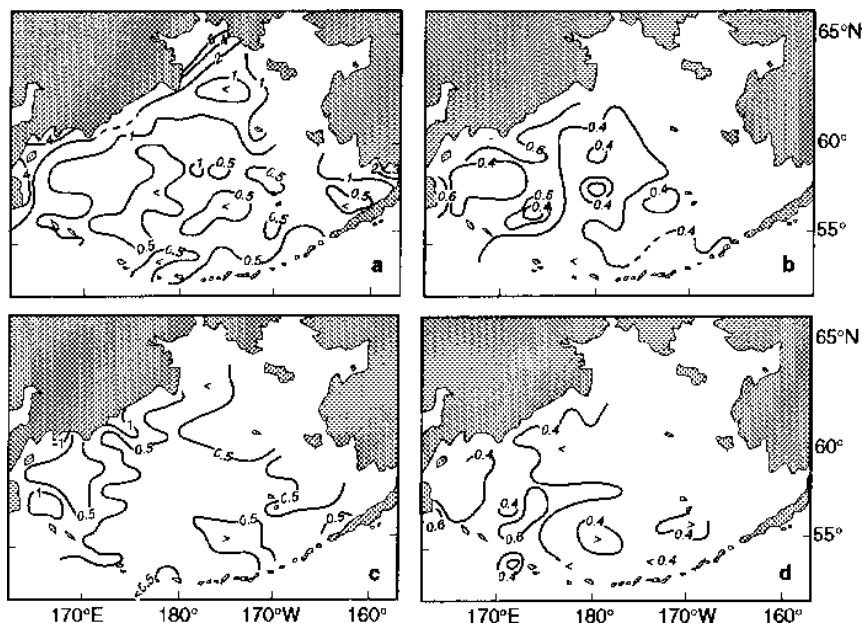


Figure 15. Variability of salinity (ppt) at a depth of: (a) at the surface, (b) 50 m, (c) 100 m, and (d) 150 m.

Island passes, minimum salinity is frequently in August-September (Fig. 14).

The greatest range of salinity variation is observed in the surface layer (Fig. 15). The largest values (up to 4-7 ppt) occur toward the periphery of the sea. In the deep basin, the annual salinity variation is less than 1 ppt. Minimum variability is observed near the Aleutian passes (Fig. 15). At a depth of 50 m (Fig. 15b), the main pattern in the annual salinity variation is similar to that at the surface, but the magnitude is less. At a depth of 100 m, there is a further decrease in the annual salinity variability (Fig. 15c). Even at the periphery of the sea, variability at this depth barely exceeds ~1 ppt. At a depth of 150 m, the difference in the magnitudes of salinity variability divides the sea into two regions (Fig. 15d). In the eastern section, annual salinity variability is small (0.2-0.4 ppt), while in the west variability is larger (0.4-0.6 ppt).

### ***Spatial and Temporal Distribution of Salinity***

The major large-scale features in the distribution of salinity in the surface layer are preserved throughout the year. Pacific Ocean water generally has the highest salinity. The salinity decreases approaching the coast, especially

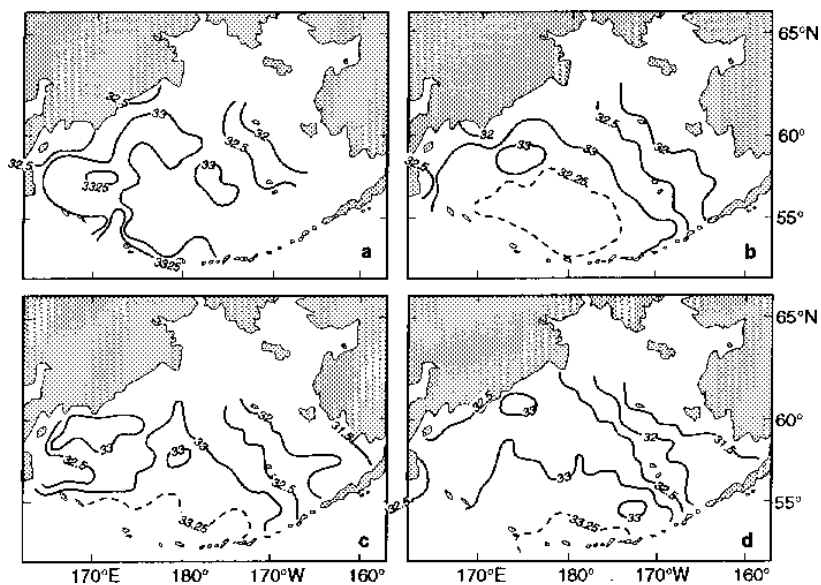


Figure 16. Salinity (ppt) distribution at the surface of the Bering Sea in: (a) January, (b) February, (c) March, and (d) April.

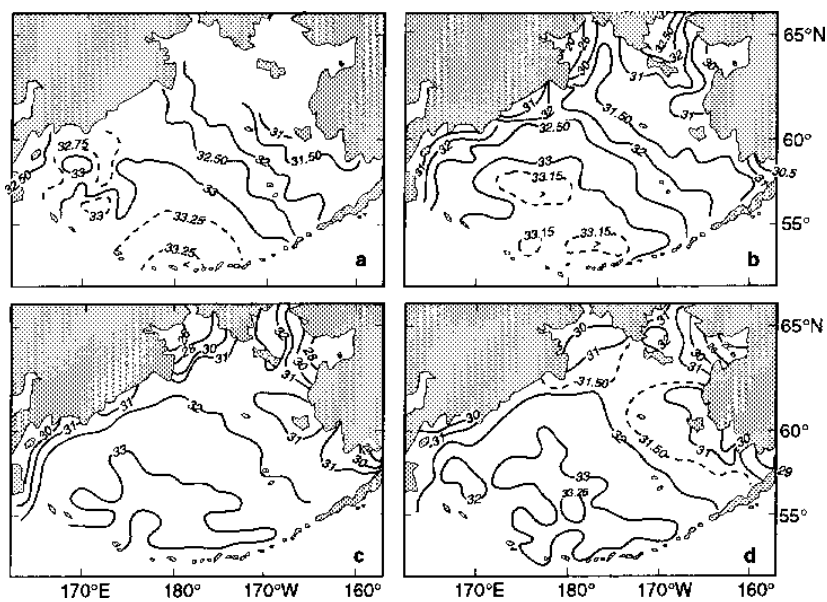


Figure 17. Salinity (ppt) distribution at the surface of the Bering Sea in: (a) May, (b) June, (c) July, and (d) August.

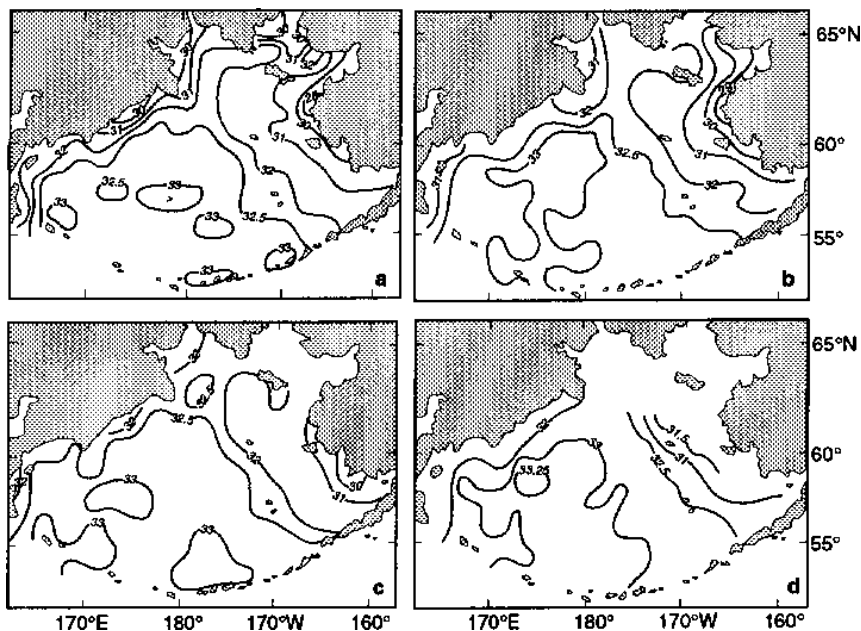


Figure 18. Salinity (ppt) distribution at the surface of the Bering Sea in: (a) September, (b) October, (c) November, and (d) December.

on the eastern Bering Sea shelf. A pronounced frontal zone divides the shelf waters from waters over the deep basin (Figs. 16-18). The lowest surface salinities are observed at the head of the Gulf of Anadyr (as low as 19-20 ppt), in Norton Sound (<29 ppt), and in Bristol Bay (as low as 30 ppt) in June-July (Fig. 17b,c). River input is less important along the Kamchatka coast, so that salinity in that region does not fall below ~30.5 ppt. The shapes of the 31.5 ppt and 32.0 ppt isohalines illustrate the flow of Pacific Ocean water onto the shelf east of Cape Navarin (Fig. 17b).

Near the Aleutian Islands (east of 176°E), a region of reduced salinity begins to form in June (Fig. 17b). Its formation is associated with continental runoff in the Gulf of Alaska as well as from the Aleutian Islands. The freshening of nearshore surface water is generally greatest in July (Fig. 17c). There is about a month lag between the peak river runoff in June and the minimum salinity of the shelf waters in July. In the deep basin of the Bering Sea, the change in salinity from June to July is <0.1 ppt. In October and November, the positions of the 32.0 and 32.5 ppt isohalines indicates the path of high-salinity water which flows along the outer edge of the Gulf of Anadyr toward Chirikov (Anadyr) Strait and also to the south of St. Lawrence Island (Fig. 18b).

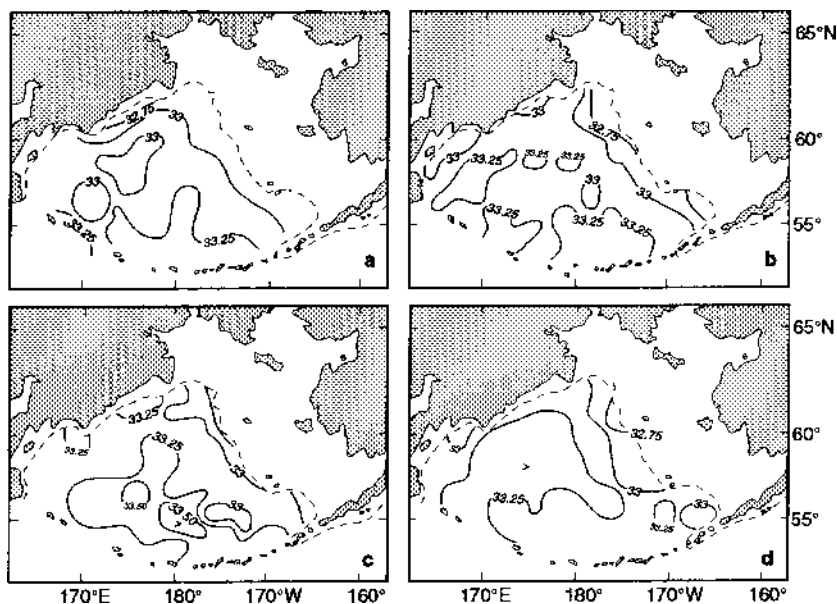


Figure 19. Salinity (ppt) distribution at 100 m in: (a) March, (b) May, (c) August, and (d) October.

At a depth of 50 m, all the main large-scale features of the surface salinity distribution are maintained. The characteristic features of the salinity field are a weak reflection of the surface distribution. The salinity at 50 m varies little during the course of the year. The smallest variability occurs on the eastern Bering Sea shelf. This is linked to the low current speeds and the sharp pycnocline between the surface and underlying waters. In the Gulf of Anadyr in October, at the start of autumn convection, salinities decrease to 32.8 ppt. The frontal zone dividing the shelf from the deep basin is observed all year long, although from September to November gradients in the zone decrease.

The salinity field at 100 m and 200 m (Figs. 19, 20) is subject to the influence of surface variations in salinity mainly in the Aleutian passes. This process is most clearly observed in October. In the other parts of the sea, salinity variability during the course of the year is linked to features in the large-scale circulation.

The distribution of salinity at 500 m and 1,000 m (Fig. 21) reflects the entry of Pacific Ocean water into the Bering Sea through the deep passes of the western part of the Aleutian Islands. Salinity is highest in areas adjoining these passes. As Pacific Ocean water spreads into the deep basin, its salinity is slightly and gradually decreased (Fig. 21a,b). At depths



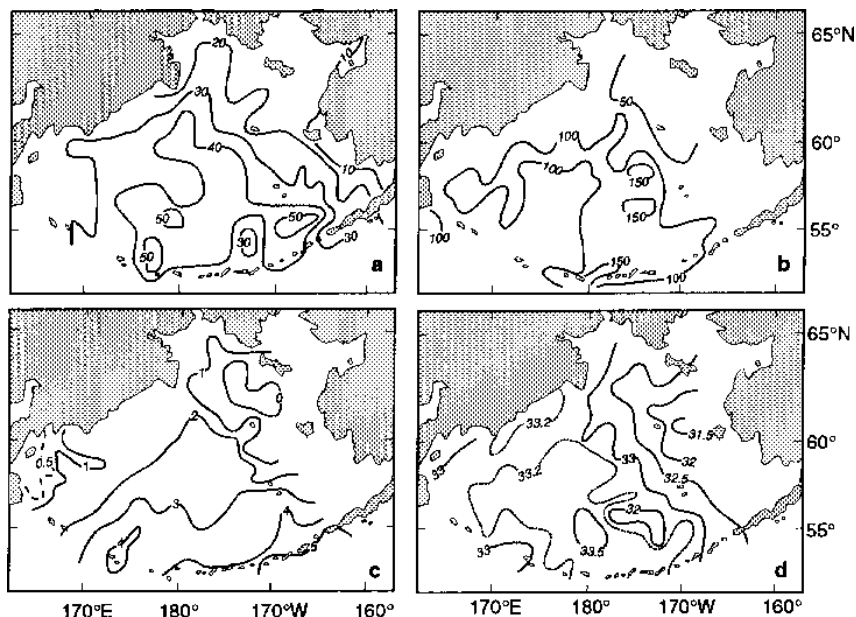


Figure 22. Characteristics of the intermediate Bering Sea water mass in summer: (a) location of the upper boundary in meters, (b) depth of the core of the water mass, in meters, (c) temperature ( $^{\circ}\text{C}$ ) of the core, and (d) salinity (ppt) of the core.

of 2,000 m and 3,000 m (Fig. 21c,d), it is difficult to distinguish a prevailing pattern.

## Characteristics of Water Masses

Water masses in the upper layer of the sea are influenced by river runoff, advection of water from the Pacific Ocean, solar radiation, evaporation, precipitation, wind mixing, autumn and winter convection, the formation and destruction of ice, spreading of characteristics by currents, and turbulent mixing. At intermediate and deep depths, the dominant effects are water exchange with the Pacific Ocean and mixing of water by currents.

Warming and freshening of the surface water in the spring allow the formation of the upper boundary of the intermediate Bering Sea water mass (IBWM). The upper boundary of the IBWM in summer is shown in Figure 22a. The core of IBWM is deepest in regions of inflow of Pacific Ocean water and also in the region just west of the eastern shelf (Fig. 22b). Near the shelf break, there are large horizontal salinity gradients. However, the general large-scale pattern of its distribution is maintained. The

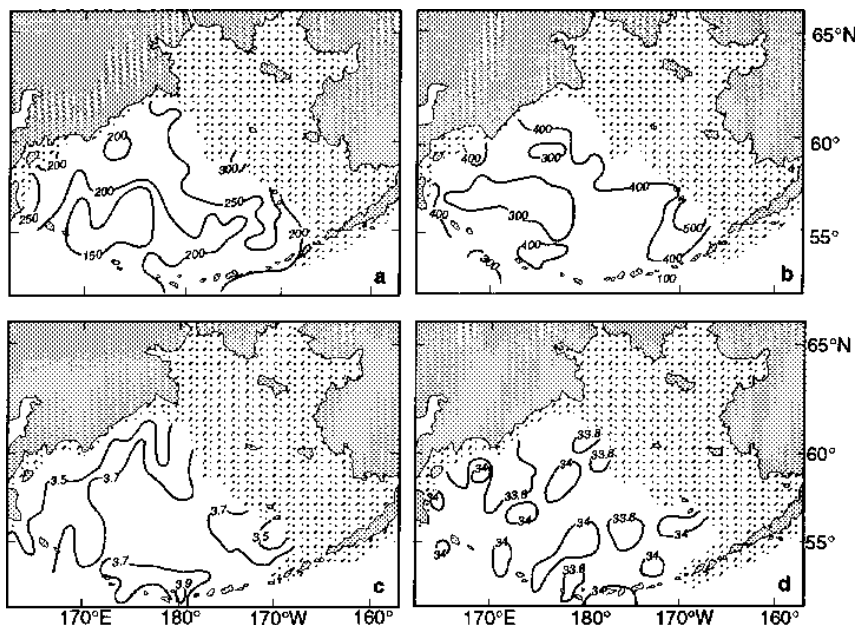


Figure 23. Characteristics of the intermediate Pacific Ocean water mass in August: (a) location of the upper boundary in meters, (b) depth of the core of the water mass, in meters, (c) temperature ( $^{\circ}\text{C}$ ) of the core, and (d) salinity (ppt) of the core. (The hatched area is shallower than the water mass).

only change is in its core temperature. The highest temperatures (up to  $5^{\circ}\text{C}$ ) are noted in the straits in the central and eastern parts of the Aleutian Islands, while temperatures near the coast of Kamchatka are  $<1^{\circ}\text{C}$ . The lowest core temperatures ( $<0^{\circ}\text{C}$ ) are distinguished in the anticyclonic eddy south of St. Lawrence Island (Fig. 22c). The salinity at the core of the IBWM in summer varies from 31.5 to 33.5 ppt (Fig. 22d).

The main feature of the intermediate Pacific Ocean water mass (IPWM) is its high temperature. There is little seasonal variation in its characteristics. Its upper boundary gradually deepens from March, the time of maximum cooling, through October, the start of the next cycle of cooling of the surface water. The core of the IPWM occurs at depths from 200 to 500 m, with maximum core depths occurring at the periphery of the deep basin (Fig. 23b). The temperature at the core of the IPWM varies within narrow limits (from  $3.4^{\circ}$  to  $4.0^{\circ}\text{C}$ ; Fig. 23c). The highest temperatures occur where Pacific Ocean water enters the Bering Sea. The lowest values ( $3.4$ – $3.5^{\circ}\text{C}$ ) are noted near the Kamchatka coast, associated with severe cooling of water there in the winter. The salinity at the core of the IPWM

varies from 33.7-34.1 ppt (Fig. 23d). The maximum values in winter, spring, and summer are seen where Pacific Ocean water enters the Bering Sea, as well as near the coast of the Kamchatka Peninsula. In autumn, in dynamically active regions (the Aleutian Island passes and a section of the northeast slope) the core salinity of the IPWM is minimal because of mixing with fresher overlying water.

The deep water mass (DWM) is the most homogeneous in its characteristics. It has lower temperatures and higher salinities than the intermediate Pacific Ocean water mass. The upper boundary of the DWM is shallowest in regions of inflow of Pacific Ocean water and at the periphery of the deep part of the sea. The core of the deep water mass is near the bottom, in the deep part of the Bering Sea. Water temperature at depths below 3,000 m is 1.45-1.65°C, while salinity is 34.60-34.68 ppt.

## Acknowledgments

We thank Sigrid Salo (NOAA/PMEL) for her many efforts in translation and preparation of this manuscript.

## References

- Arsenev, V.S. 1967. Currents and water masses of the Bering Sea. Nauka, Moscow. 135 pp.
- Barnes, C.A., and T.G. Thompson. 1938. Physical and chemical investigations in the Bering Sea and portions of the North Pacific Ocean. University of Washington Publication in Oceanography 3(2):1-164.
- Belkin, I.M. 1984. An assessment of editing oceanographic data (main principles). Trudy Vse Nauchno-Issledobatel'skogo Instituta Gidrometeorologicheskogo Informatsia-Mirny Danny Tsentr 113:108-113.
- Burkov, V.A. 1958. The hydrography of the Komandoro-Kamchatka region of the Pacific Ocean in spring. Trudy Instituta Okeanologii Akademii Nauk SSSR 27:12-21.
- Coachman, L.K. 1979. On lateral water mass interaction: A case study, Bristol Bay, Alaska. Journal of Physical Oceanography 9:278-297.
- Coachman, L.K. 1986. Circulation, water masses, and fluxes on the southeastern Bering Sea shelf. Continental Shelf Research 5:23-108.
- Coachman, L.K., and R.L. Charnell. 1977. Fine structure in outer Bristol Bay. Deep-Sea Research 24:869-889.
- Coachman, L.K., K. Aagaard, and R.B. Tripp. 1975. Bering Strait: The Regional Physical Oceanography. University of Washington Press, Seattle. 172 pp.
- Coachman, L.K., T.H. Kinder, J.D. Schumacher, and R.B. Tripp. 1980. Frontal systems of the southeastern Bering Sea Shelf. In: T. Castens and T. McClimans (eds.), Stratified flows, the second IAHR symposium, Trondheim, June 1980. Tapir, Trondheim, pp. 917-933.

- Davydov, I.V. 1972. On the question of oceanographic factors affecting the yield of individual generations of herring in the western Bering Sea. *Izvestia TINRO* 82:281-307.
- Davydov, I.V. 1984. On the development of oceanographic conditions in the main fisheries regions of the Far Eastern Seas. *Izvestia TINRO* 109:3-17.
- Davydov, I.V., and F.F. Lipetskiy. 1970. The hydrography of the Karaginskiy and Olyutorskiy-Karaginskiy fisheries regions in the Bering Sea. *Izvestia TINRO* 73:178-193.
- Dobrovolskiy, A.D., and V.S. Arsenev. 1961. Hydrographic characteristics of the Bering Sea. *Trudy Instituta Okeanologii Akademii Nauk SSSR* 38:64-96.
- Dobrovolskiy, A.D., A.S. Ionin, and G.B. Udintsev. 1959. The history of research in the Bering Sea. *Trudy Instituta Okeanologii Akademii Nauk SSSR*. 29:5-20.
- Dodimead, A.J., F. Favorite, and T. Hirano. 1963. Salmon of the North Pacific Ocean. Part 2, Review of Oceanography of the Subarctic Pacific Region. *Bulletin of the North Pacific Fisheries Commission* 13. 195 pp.
- Dowling, G. 1962. Subsurface horizontal temperature gradients and fluctuations in the Bering Sea. *Journal of Geophysical Research* 67:5-54.
- Favorite, F. 1974. Flow into the Bering Sea through Aleutian Island passes. In: D.W. Hood and E.J. Kelley (eds.), *Oceanography of the Bering Sea, Occasional Publication Number 2*. Institute of Marine Science, University of Alaska, Fairbanks, pp. 3-37.
- Favorite, F., A.J. Dodimead, and K. Nasu. 1976. Oceanography of the subarctic Pacific region, 1960-71. *International North Pacific Fisheries Commission Bulletin*, 33. 187 pp.
- Favorite, F., J.W. Schantz, and C.R. Hebard. 1961. Oceanographic observations in Bristol Bay and the Bering Sea, 1939-1941 (USCGT Redwing). U.S. Fish and Wildlife Service Special Scientific Report, Fisheries 381. 323 pp.
- Filyushkin, B.N. 1968. Thermal characteristics of the surface layer in the Northern Pacific Ocean. *Mezhdunarodnyy Geofizicheskiy Komitet Akademii Nauk SSSR/Okeanologicheskie Issledovaniya* 19:22-69.
- Goodman, J.R., J.H. Lincoln, T.G. Thompson, and F.A. Zeusler. 1942. Physical and chemical investigations: Bering Sea, Bering Strait, and Chukchi Sea during the summers of 1937 and 1938. University of Washington, Publication in Oceanography 3(3):81-103, plus app.
- Gubenko, N.D., and Y.L. Tsipis. 1984. On the question of the formation of data bases in the computing system KOMPAS. *Trudy Vse Nauchno-Issledovatel'skogo Instituta Gidrometeorologicheskogo Informatsia-Mirny Danny Tsentra* 113:54-67.
- Hood, D.W., and J.A. Calder. 1981. *The eastern Bering Sea Shelf: Oceanography and resources*. University of Washington Press, Seattle. 520 pp.
- Hood, D.W., and E.J. Kelley. 1974. *Oceanography of the Bering Sea. Occasional Publication 2*, Institute of Marine Science, University of Alaska, Fairbanks. 623 pp.

- Hughes, F.W., L.K. Coachman, and K. Aagaard. 1974. Circulation, transport, and water exchange in the western Bering Sea. In: D.W. Hood and E.J. Kelley (eds.), *Oceanography of the Bering Sea*. Occasional Publication 2, Institute of Marine Science, University of Alaska, Fairbanks, pp. 59-98.
- Ingraham, W.J. 1981. Shelf environment. In: D.W. Hood and E.J. Calder (eds.), *The eastern Bering Sea Shelf: Oceanography and resources*. University of Washington Press, Seattle, pp. 31-52.
- Ivanenkov, V.N. 1964. *Hydrochemistry of the Bering Sea*. Nauka, Moscow. 138 pp.
- Izrael', Y.A. 1983. Research on the ecosystems of the Bering Sea. *Gydrometeoizdat*. 157 pp.
- Khen, G.V., and V.F. Voronin. 1986. Interannual oscillations at the southern edge of shelf water in the eastern Bering Sea linked with large-scale variability. *Trudy (DVNII) Dal'nye-Vostochnogo Nauchno-Issledobatel'skogo Gidro-Meteorologicheskogo Instituta* 125:10-19.
- Kihara, K., and M. Uda. 1969. Analytical studies of the mechanisms concerning the formation of demersal fishing grounds in relation to the bottom water masses of the eastern Bering Sea, Part 1. *Tokyo University of Fisheries* N55(2):83-90.
- Kinder, T.H. 1977. The hydrographic structure over the continental shelf near Bristol Bay, Alaska, June 1976. Department of Oceanography Technical Report M773, University of Washington. 61 pp.
- Kinder, T.H., and L.K. Coachman. 1978. The front overlying the continental slope in the eastern Bering Sea. *Journal of Geophysical Research* 83:4551-4559.
- Kinder, T.H., and J.D. Schumacher. 1981. Hydrographic structure over the continental shelf of the southeastern Bering Sea. In: D.W. Hood and E.J. Calder (eds.), *The eastern Bering Sea shelf: Oceanography and resources*. University of Washington Press, Seattle, pp. 31-52.
- Kitano, K. 1970. A note on the thermal structure of the eastern Bering Sea. *Journal of Geophysical Research* 75:1110-1115.
- Kitani, K., and S. Kawasaki. 1979. Oceanographic structure in the region of the eastern Bering Sea. Part 1: The movement and physical characteristics of water in summer 1978. *Bulletin of the Far Seas Fisheries Research Laboratory* 17:1-12. (In Japanese.)
- Koto, H., and T. Fuji. 1958. Structure of the waters in the Bering Sea and Aleutian region. *Bulletin of the Fisheries Department, Hokkaido University* 9:149-170.
- Koto, H., and T. Maeda. 1965. On the movement of fish: Shoals and the change of bottom temperature on the trawl-fishing grounds of the eastern Bering Sea. *Bulletin of the Japanese Society of Scientific Fisheries* 1:263-268. (In Japanese.)
- Lazo, A.V. 1971. Several features of the hydrographic regime of the coastal zones of Bering and Medniy Islands. *Sbornik Rabot Petropavloskoi Gidro-Meteorologicheskogo Organizatsii* 1:65-76.
- Leonov, A.K. 1947. Water masses of the Bering Sea and currents at its surface. *Meteorologiya i Gydrologiya* 2:51-66.

- Leonov, A.K. 1960. Regional oceanography. Part 1: The Bering Sea. *Gidrometeoizdat*, Leningrad. 765 pp.
- Maeda, T, T. Fujii, and K. Masuda. 1968. On the annual fluctuation of oceanographic conditions in the summer. Part 2, Studies of the trawl-fishing grounds in the eastern Bering Sea. *Bulletin of the Japanese Society of Scientific Fisheries* 34:502-510. (In Japanese.)
- Milyeiko, G.N. 1973. Forecasting water temperature distribution and the position of the ice edge in the Bering Sea during the cold part of the year. *Trudy Gydro-Meteorologicheskogo Tsentra SSSR* 127:100-104.
- Mishima, S., and S. Nishizawa. 1955. Report on hydrographic investigations in Aleutian waters and the southern Bering Sea in the early summers of 1953 and 1954. *Bulletin of the Faculty of Fisheries, Hokkaido University* 6:85-124.
- Mofjeld, H.O. 1986. Observed tides on the northeastern Bering Sea Shelf. *Journal of Geophysical Research* 91:2593-2606.
- Moisyeev, L.K. 1978. Stratification of the temperature field. *Trudy Vse Nauchno-Issledobatel'skogo Instituta Gydrometeorologicheskogo Informatsia-Mirny Danny Tsentra* 45:36-62.
- Muench, R.D. 1976. A note on eastern Bering Sea shelf hydrographic structure, August 1974. *Deep-Sea Research* 23:245-247.
- Muench, R.D., R.B. Tripp, and J.D. Cline. 1981. Circulation and hydrography of Norton Sound. In: D.W. Hood and J.A. Calder (eds.), *The eastern Bering Sea Shelf: Oceanography and resources*. University of Washington Press, Seattle, pp. 77-93.
- Natarov, V.V. 1963. On water masses and currents in the Bering Sea. *Trudy Vladivostochno Nachno-Issledobatel'skogo Rybnogo Organizatsii* 48:111-133.
- Naumov, G.K., and Y.A. Khistyayev. 1972. Some features in the hydrography near the shelf break in the Bering Sea. In: *Trudy All-Union Hydromet Service of the USSR, Oceanographic Forecasting and Calculations, Gidrometeoizdat*, Leningrad, pp. 95-102.
- Ohtani, K. 1969. On the oceanographic structure and ice formation on the continental shelf in the eastern Bering Sea. *Bulletin of the Faculty of Fisheries, Hokkaido University* 20:94-117.
- Ohtani, K. 1973. Oceanographic structure in the Bering Sea. *Memoirs of the Faculty of Fisheries, Hokkaido University* 21:65-106.
- Otobe, H., T. Nakai, and A. Hattori. 1983. Heat energy exchange across the sea surface of the Bering Sea and the North Pacific Ocean in summer: Estimates from direct measurements of radiation fluxes. *Deep-Sea Research* 30:1023-1031.
- Pereskokov, A.I. 1984. Elimination of spikes during statistical processing of deep hydrometeorological data. *Trudy Vse Nauchno-Issledobatel'skogo Instituta Gydrometeorologicheskogo Informatsia-Mirny Danny Tsentra* 101:106-113.

- Poluektov, S.V., and Y.A. Khistyayev. 1981. Thermal stratification of the active layer of the Bering Sea in winter. *Trudy Vse Nauchno-Issledobatel'skogo Instituta Gydrometeorologicheskogo Informatsia-Mirny Danny Tsent* 83:15-23.
- Rathburn, R. 1894. Summary of the fishing investigations conducted in the North Pacific Ocean and Bering Sea from July 1, 1888 by the U.S. Fish Commission Steamer "Albatross." *Bulletin of the U.S. Fisheries Commission* 12:127-201.
- Ratmanov, G.E. 1937. On the hydrology of the Bering and Chukchi seas. *Issledobaniya Moryei* 25:10-118.
- Reed, R.K. 1978. The heat budget of a region in the eastern Bering Sea, summer 1976. *Journal of Geophysical Research* 33:3636-3645.
- Saur, J.F.T, R.M. Lesser, A.J. Carsola, and W.M. Cameron. 1952. Oceanographic cruise to the Bering and Chukchi seas, summer 1949. U.S. Navy Electronics Laboratory Report 298. San Diego, CA. 38 pp.
- Sayles, M.A, K. Aagaard, and L.K. Coachman. 1979. Oceanographic atlas of the Bering Sea Basin. University of Washington Press, Seattle. 158 pp.
- Schumacher, J.D., T.H. Kinder, D.J. Pashinski, and R.L. Charnell. 1979. A structural front over the continental shelf of the eastern Bering Sea. *Journal of Physical Oceanography* 9: 79-87.
- Swift, J.H., and K. Aagaard. 1976. Upwelling near Samalga Pass. *Limnology and Oceanography* 21:399-408.
- Takenouti, A.Y. 1976. Recent Japanese physical oceanographic studies of the Bering Sea. *Marine Science Communications* 2:285-297.
- Takenouti, A.Y., and K. Ohtani. 1974. Currents and water masses in the Bering Sea: A review of Japanese work. In: D.W. Hood and E.J. Kelley (eds.), *Oceanography of the Bering Sea*. Occasional Publication Number 2, Institute of Marine Science, University of Alaska, Fairbanks, pp. 39-57.
- Tanner, Z.L. 1890. Explorations of the fishing grounds of Alaska, Washington Territory, and Oregon during 1888 by the U.S. Fish Commission Steamer "Albatross." *Bulletin of the U.S. Fisheries Commission* 8:1-92.
- Tiguntsev, L.A. 1971. Variability of water temperature in the region of Bering Strait. *Trudy Articheskogo i Antarticheskogo Nauchno-Issledobatel'skogo* 302:50-57.
- Yarichin, V.G. 1984. Water structure and water masses in the Bering Sea in the summer of 1982. *Trudy (DVNII) Dal'nye-Vostochnogo Nauchno-Issledobatel'skogo Gydro-Meteorologicheskogo Instituta* 111:83-97.



## CHAPTER 4

# Bering Sea Tides

**Zygmunt Kowalik**

*Institute of Marine Science, University of Alaska Fairbanks, Fairbanks, Alaska*

## Abstract

This paper includes a review of research on tides in the Bering Sea and presents new results obtained from numerical models. The focus of investigations is a description of the enhanced tidal currents. Dynamics of the tidal currents are shown to be closely related to the tidal period. In both semidiurnal and diurnal bands of oscillations the tides travel from the North Pacific through the deep basin onto the shelf. The enhanced tidal currents for both bands of oscillations are generated due to topographic amplification. Examples of such amplification occur during propagation of tides from deep to shallow water over the continental shelf slope, in proximity to the land and islands and also in the narrow passages and straits. The most conspicuous topographic enhancement occurs in the triangular-shaped Bristol Bay where  $M_2$  tide current increases to about 100 cm/s. In the diurnal band of oscillation, the enhanced currents are generated not only due to the topographic amplification but also due to the tidal shelf waves trapped against the continental shelf slope. Numerical computations and observations are applied to identify diurnal tidal currents related to the trapped shelf waves. Investigations reveal two major regions of diurnal tide enhancement: (a) off Cape Navarin, and (b) close to the Aleutian Islands between 170°W and 173°W. Regions of lesser diurnal tide enhancement are located along the shelf break where diurnal tides depict local maxima in the sea level distribution. Nonlinear interactions of the strong tidal currents also have been investigated. To study tidal current rectification over the bottom topography, a high-resolution numerical model was used in the region of the Pribilof Islands and Canyon. The existence of the model's residual currents is well corroborated by long-term time series obtained around St. Paul Island. Six current meters deployed for up to 1 year revealed a very stable clockwise flow in the range 4 to 18 cm/s.

## Introduction

Tides provide the most important and consistent driving force in the Bering Sea. The tides and tidal currents on the Bering Sea shelf play an important

role in such oceanographic processes as the maintenance of the density structure, sediment resuspension and transport, and the distribution of benthic and intertidal organisms. Observations in the Bering Sea described four hydrographic domains separated by three fronts (Kinder and Schumacher 1981; Schumacher and Stabeno 1998): coastal, middle shelf, outer shelf, and oceanic. Basic processes influencing fronts are tides, wind, and thermohaline circulations. The role of the tides in generating a coastal domain of uniform vertical distribution of salt and temperature is well understood. The role of tidal motion in sustaining middle shelf, outer shelf, and shelf break circulation needs further investigation. The kinetic energy of the tidal flow over middle and outer shelves is much greater than the kinetic energy of the mean flow. For example, Kinder and Schumacher (1981) showed that at the middle shelf in Bristol Bay the mean flow is about 2 cm/s while tidal currents attain 20 cm/s. Tidal currents can play an especially important role in the material transport between shelf edge and deep ocean. Depending on interaction with bathymetry, both upwelling and downwelling are feasible; therefore these processes either bring nutrients into the surface layer or transport particulate matter from the shelf into the deep ocean. This transport process was investigated by Yanagi et al. (1992) and is called "tidal pump." It can be important in explaining the shelf-deep water interaction in the Bering Sea.

The tides enter the Bering Sea as progressive waves from the North Pacific Ocean, principally through the central and western passages of the Aleutian-Commander Islands. The Arctic Ocean is a secondary source of tides. Therefore, tides in the Bering Sea are considered to be the result of co-oscillation with the Pacific and, to a lesser degree, with the Arctic Ocean. These tides are dominated by four constituents:  $M_2$ ,  $N_2$ ,  $K_1$ , and  $O_1$ . Observations show that over most of the shelf the tides are primarily semidiurnal. The diurnal tides are dominant, however, in proximity to the  $M_2$  amphidromic points, in Norton Sound, at some locations along the shelf break, and near some Aleutian Islands. Pearson et al. (1981) constructed empirical charts for four major tidal constituents ( $M_2$ ,  $N_2$ ,  $K_1$ , and  $O_1$ ) over the Bering Sea shelf. Mofjeld (1984, 1986) and Mofjeld et al. (1984) analyzed data for three diurnal components ( $O_1$ ,  $P_1$ ,  $K_1$ ) and three semidiurnal components ( $M_2$ ,  $S_2$ ,  $N_2$ ) over the northeastern Bering shelf and made extensive comparisons against numerical models and tidal theory.

Several numerical models have been applied to Bering Sea tides. They are of two basic types: vertically integrated models and three-dimensional models which simulate vertical structure of tidal currents. The vertically integrated models were applied to the Bering Sea shelf by Hastings (1976) and to the entire Bering Sea by Sunderman (1977). Three-dimensional models were built to simulate the tides in the Alaskan coastal waters by Liu and Leendertse (1979, 1981, 1982, 1990). A direct tidal analysis of the altimetry from the Geosat Exact Repeat Mission was carried out for the Bering Sea and other regional seas by Cartwright et al. (1991). These data have a spatial resolution of about 100 km. Recent world tide models by LeProvost et

al. (1994) and Kantha (1995) include the Bering Sea domain with much finer spatial resolution. The model by Kantha (1995) has approximately 22 km resolution and specifically discusses  $M_2$  and  $K_1$  tides in the Bering Sea. The Russian investigations are summarized by Bogdanov et al. (1991).

The difference in the periods between diurnal and semidiurnal tidal waves results in the different dynamics of the tide propagation. Tidal waves can depict several different behaviors. Gravity, Coriolis force, and bathymetry play the major role in tidal dynamics. If gravity is the major restoring force, then the tide wave's local amplification may occur due to resonance in the local embayment adjacent to the open sea basin. The condition for resonance to occur in such a basin is that its length must be a quarter of the wavelength of the oscillation forced from outside. Quite different behavior of the tidal wave can occur under the influence of the Coriolis force, gravity, and bathymetry. Here the resonance condition may lead to so-called topographic waves. Tidal waves propagating into continental slope and shelf areas locally induce topographic waves where the local period of rotational-gravitational mode is equal to the tidal period. Tidally generated topographic waves occur only in the regions poleward from the critical latitude (i.e., the latitude where inertial period is equal to the tidal period). This latitude for the  $K_1$  tide is 30, and for the  $M_2$  tide is 74.5. Therefore, in the Bering Sea domain only diurnal topographic waves can be generated.

The important features of tidal dynamics I will examine and define here are:

- (a) Distribution of enhanced currents in the semidiurnal band of periods. These often occur in shallow water, resulting in enhanced local mixing and tidal fronts.
- (b) Distribution of the tidal currents and regions of near-resonant trapped tidal waves in the diurnal band of periods. Trapped tidal waves often occur at the edges of continental shelves. Therefore, they are important in the dynamical coupling and exchange of properties between shelf and deep ocean.
- (c) Position and patterns of the residual currents. These currents occur permanently along horizontal and vertical directions. Often, along the horizontal direction, the residual motion occurs as clockwise and counterclockwise eddies. Residual currents play a considerable role in both small and mesoscale transport of nutrients and plankton in shallow water and between shelf and deep waters.

Important mechanisms of tidal current enhancement are internal waves and, especially, large amplitude internal wave packets. This field of research is under development in the Bering Sea; a few measurements and three-dimensional models by Liu and Leendertse (1990) indicate that tidal signal is of both barotropic and baroclinic origin.

I will also extend the investigations of Pearson et al. (1981), Mofjeld (1984, 1986), Mofjeld et al. (1984), and Liu and Leendertse (1979, 1981, 1982, 1990) on tides in the eastern part of the Bering Sea to the whole Bering Sea. Further, some new results on tidal current distribution will be given, and the geographic regions of enhanced currents will be delineated.

## Tidal Equations and Parameters

Information on tides and tidal currents in the Bering Sea has been given in several papers which describe observations and numerical modeling. This information is mainly related to the Bering Sea shelf. The Bering Sea is too vast to be covered by a dense net of tidal observations and at present the amount of data is not sufficient to draw cotidal charts. On the other hand, the resolution given by the numerical model is sufficient to depict well-resolved tidal charts which can be compared against data. Measurements derived in the Bering Sea provide the possibility to test and validate model performance, but unfortunately, only at a few locations. A numerical model is used here as a unifying tool which will bring all investigations under one umbrella, although the numerical model also has inherent problems influencing its reliability. The main parameters which define a model's performance are resolution (defined by horizontal grid spacing) and bathymetry. I began computation in the entire Bering Sea with a resolution of about 10 km because this resolution is sufficient to describe tidally generated trapped shelf waves (Kowalik and Proshutinsky 1993). Even so, it does not resolve fully the nonlinear tidal interactions. Zimmerman (1978) and Robinson (1981) suggested that the tidal ellipse (tidal excursion) length ought to be resolved for the proper investigation of the nonlinear terms. Often tidal excursion of the water particle is on the order of several kilometers. This limits resolution to several hundred meters. In the Bering Sea high resolution bathymetry is available only around islands and close to the Alaska shoreline. In vast areas of the Bering shelf and in the deep basin, the bathymetry is poorly known.

The model domain includes the Bering Sea and a small portion of the North Pacific, from 48°N to 67°N and from 154°E to 142°W (Fig. 1). The Bering Sea bathymetry structure displays two large domains of importance for the tidal dynamics: deep domain (>3,000 m) located southwest and shallow domain located northwest. The depth distribution for the numerical model is based on an ETOPO5 file with many corrections compiled from the available charts. The compiled depth distribution and the major areas of interest are shown in Fig. 1. To study nonlinear effects, I chose a domain around the Pribilof Islands. Here the fine horizontal grid step will be introduced and afterward, around one of the islands (St. Paul Island), a super-fine grid will be used to obtain results for comparison against measurements (Kowalik and Stabeno submitted). Investigation of the high resolution tides began around St. Paul Island by analyzing the

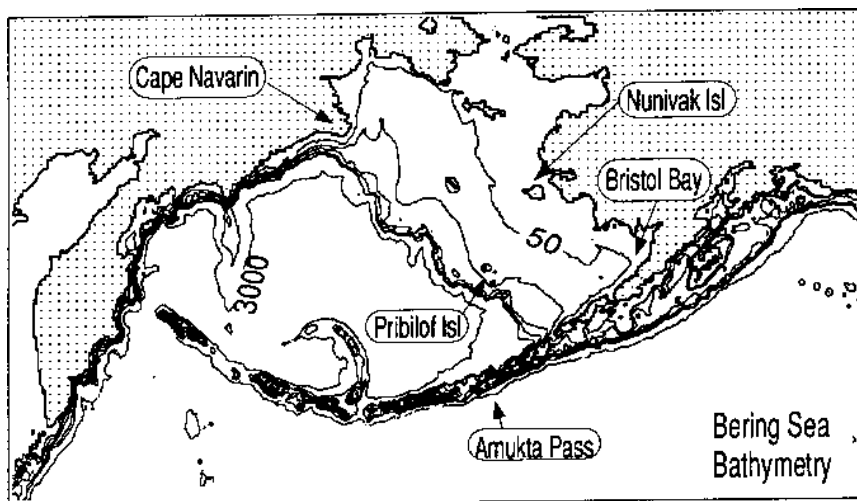


Figure 1. Bering Sea bathymetry.

large-scale model of the entire Bering Sea with resolution of 5 minutes along latitude and 10 minutes along longitude (Fig. 2). At the latitude of 60°N both steps are equal to 9.26 km; therefore I use this distance to describe the large-scale numerical lattice. In the entire Bering Sea a spherical system of coordinates is used. The results of computations from this domain serve for construction of the boundary conditions for the domain around the Pribilof Islands (Fig. 2). The resolution applied in the Pribilof Islands domain is close to 1.852 km and the rectangular system of coordinates is used. I have applied the results of computations from the latter domain to establish boundary conditions for the computations around St. Paul with the grid size of 617 m.

To obtain the distribution of tide amplitudes and phases, I used the vertically integrated equations of motion and continuity in the spherical coordinate system (Gill 1982):

$$\frac{Du}{Dt} - fv - \frac{uv \sin \phi}{R \cos \phi} = -\frac{g}{R \cos \phi} \frac{\partial}{\partial \lambda} (\alpha \zeta - \beta \zeta_0) - \frac{\tau_{\lambda}^b}{\rho H} + Au \quad (1)$$

$$\frac{Dv}{Dt} + fu + \frac{uv \sin \phi}{R \cos \phi} = -\frac{g}{R} \frac{\partial}{\partial \phi} (\alpha \zeta - \beta \zeta_0) - \frac{\tau_{\phi}^b}{\rho H} + Av \quad (2)$$

$$\frac{\partial \zeta}{\partial t} + \frac{1}{R \cos \phi} \frac{\partial (Hu)}{\partial \lambda} + \frac{1}{R \cos \phi} \frac{\partial}{\partial \phi} (Hv \cos \phi) = 0 \quad (3)$$

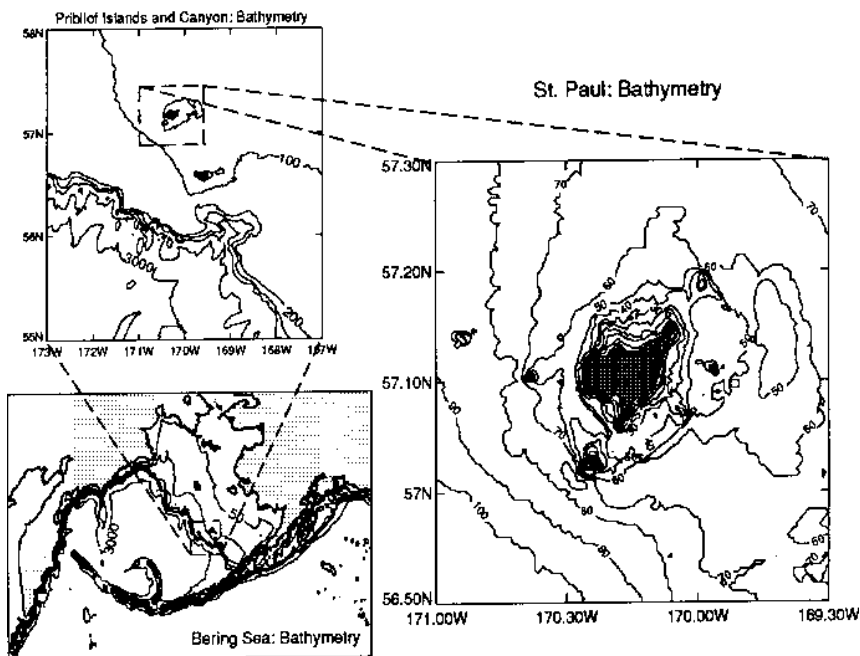


Figure 2. Computational domains and bottom topography. Bering Sea: grid resolution 9.26 km. Pribilof Islands and Canyon: grid resolution 1.852 km. St. Paul Island: grid resolution 0.617 km.

Here

$$\frac{D}{Dt} = \frac{\partial}{\partial t} + \frac{u}{R \cos \phi} \frac{\partial}{\partial \lambda} + \frac{v}{R} \frac{\partial}{\partial \phi} \quad (4)$$

The advective nonlinear terms in equation (4) are about two orders of magnitude larger than the remaining nonlinear terms in equations (1) and (2); therefore only advective nonlinear terms are taken into account in the ensuing computations.

The operator in the horizontal friction term in equation (1) and (2) is

$$A = N_h \left[ \frac{1}{R^2 \cos^2 \phi} \frac{\partial^2}{\partial \lambda^2} + \frac{1}{R^2 \cos \phi} \frac{\partial}{\partial \phi} \left( \cos \phi \frac{\partial}{\partial \phi} \right) \right] \quad (5)$$

The bottom friction components are taken as

$$\tau_\lambda^b = \rho r u \sqrt{u^2 + v^2}; \quad \tau_\phi^b = \rho r v \sqrt{u^2 + v^2}. \quad (6)$$

In equation (6)  $r$  denotes the bottom drag coefficient; it will be taken as  $r = 2.6 \times 10^{-3}$ .

The following notations have been used in the above equations:

- $\lambda, \phi$  = longitude and latitude
- $t$  = time
- $\zeta$  = free surface elevation
- $u$  = velocity component along longitude
- $v$  = velocity component along latitude
- $\rho$  = water density
- $N_h$  = horizontal eddy viscosity
- $H$  = depth (does not include sea level)
- $f$  = Coriolis parameter
- $g$  = gravity acceleration
- $R$  = radius of the earth
- $\zeta_0$  = the equilibrium tide
- $\alpha, \beta$  = parameters accounting for tidal potential perturbations.

Seven tidal constituents, namely  $K_1$ ,  $O_1$ ,  $P_1$ ,  $Q_1$ ,  $M_2$ ,  $N_2$ , and  $S_2$ , are included in the computations. Generation of the tidal constituents is done through the open boundaries of the computational domain and through astronomical forcing given in equations (1) and (2). The boundary condition at the coast is defined as no normal flow. This condition is easily implemented through the staggered C (Arakawa) grid. Along the open boundaries, amplitudes and phases for every tidal constituent are specified. This is accomplished through the results obtained by Kantha (1995) and Schwiderski (1979, 1981a-f). The tidal forcing is described in equations (1) and (2) through terms which are multiplied by coefficients  $\alpha$  and  $\beta$ . These terms include the tide-generating potential with various corrections due to earth tide and ocean loading (Schwiderski 1979, 1981a-f). Coefficient  $\alpha$  defines ocean loading; its value ranges from 0.940 to 0.953 according to Ray and Sanchez (1989). The term  $\beta\zeta_0$  includes both the tide-generating potential and correction due to the earth tide. It is usually expressed as (Hendershott 1977)

$$\beta\zeta_0 = (1 + k - h)\zeta_0 \quad (7)$$

Here  $k$  and  $h$  denote Love numbers, which are equal to 0.302 and 0.602, respectively. These numbers are averaged over all tidal constituents. The equilibrium tide for the diurnal constituents is

$$\zeta_0 = H_n \sin 2\phi \cos(\sigma_n t + \lambda) \quad (8)$$

Here  $H_n = 14.25$  cm for  $K_1$  and  $H_n = 10.06$  cm for  $O_1$ . For the semidiurnal constituents the equilibrium tide is

$$\zeta_0 = H_n \cos^2 \phi \cos(\sigma_n t + 2\lambda) \quad (9)$$

Here  $H_n = 24.23$  cm for  $M_2$  and  $H_n = 4.639$  cm for  $N_2$ . Hence the tide-generating terms in equation (1) and (2) can be calculated from equations (8) and (9). In the calculation process, along with the refining of the numerical grid, it is necessary to take into account the dependence of the horizontal exchange of momentum on the scale of numerical grid. The computations were carried out with  $N_h = 2.0 \times 10^7$ ,  $N_h = 5 \times 10^6$ , and  $N_h = 5 \times 10^5$  cm<sup>2</sup>/s for the space grids of 9.26 km, 1.852 km, and 617 m, respectively.

## Tides in the Bering Sea

Generation of tides in the models is accomplished by both astronomical forcing and boundary conditions. The astronomical forcing is well defined in equations (1) and (2), but the boundary conditions ought to be interpolated from available data to the fine numerical grid used. At the southern and northern boundaries the amplitudes and phases are taken from Kantha's (1995) and Schwiderski's (1979, 1981a-f) computations and from Cartwright et al. (1991). In the Kantha model a resolution of about 22 km is used. In the Schwiderski model and in satellite-derived data a resolution of 1° is used. Missing values for my numerical grid are interpolated linearly from the Kantha and Schwiderski results. At the northern boundary, which is located close to the Bering Strait, a relatively variable tidal amplitude and phase are observed. Therefore the results derived from ground observations are used together with the model data to establish boundary conditions. The computations of mixed tides (seven waves) were carried out for a 2-month period. After one month the full energy of the system became stationary. During the second month the sea level and velocity were recorded every hour for the harmonic analysis (Foreman 1978). Below, only the four major constituents are discussed— $M_2$ ,  $N_2$ ,  $K_1$ , and  $O_1$ .

Distribution of co-amplitude (continuous) lines and co-phase (dashed) lines for the principal semidiurnal lunar constituent ( $M_2$ ) is depicted in Fig. 3. The calculated distribution of amplitudes and phases is similar to the distribution derived through numerical models by Sunderman (1977), Liu and Leendertse (1979, 1981, 1982, 1990), and Kantha (1995), as well as through measurements at the shelf domain by Pearson et al. (1981). Propagation of the  $M_2$  constituent follows bathymetric division of the Bering Sea into the deep basin, where a small change in amplitude and phase occurs, and the shelf basin with many amphidromic points due to partial reflection of the tide wave in the semi-enclosed water bodies. The amplitudes increase in the narrow and shallow bays. The most conspicuous amplitude enhancement, up 150 cm, occurs in triangular-shaped Bristol Bay. All islands, small and large, introduce disturbance into otherwise smooth distribution of amplitude.

The  $M_2$  current ellipses are given in Fig. 4. Ellipses are very suitable for studying behavior of the tidal wave and performing comparison against

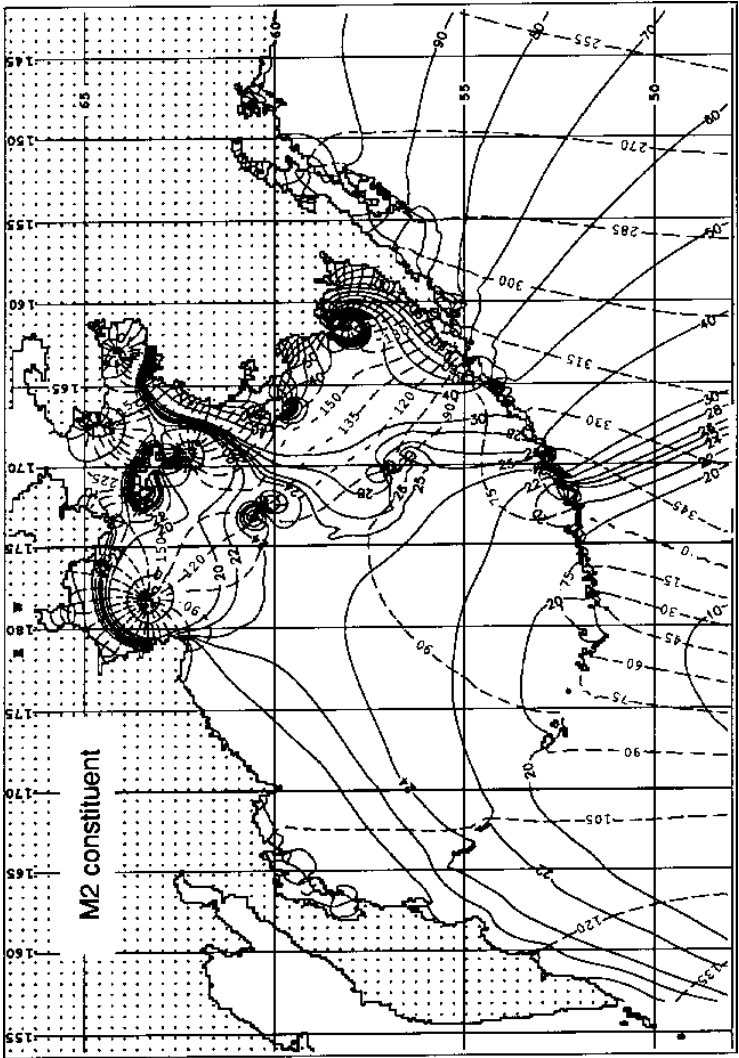


Figure 3. Computed amplitude (solid lines, in centimeters) and phase (dashed lines, in degrees) of surface elevation for the semidiurnal  $M_2$  tide, grid spacing = 9.26 km. The contours for the phase are plotted every 15°. Phase is referred to Greenwich.

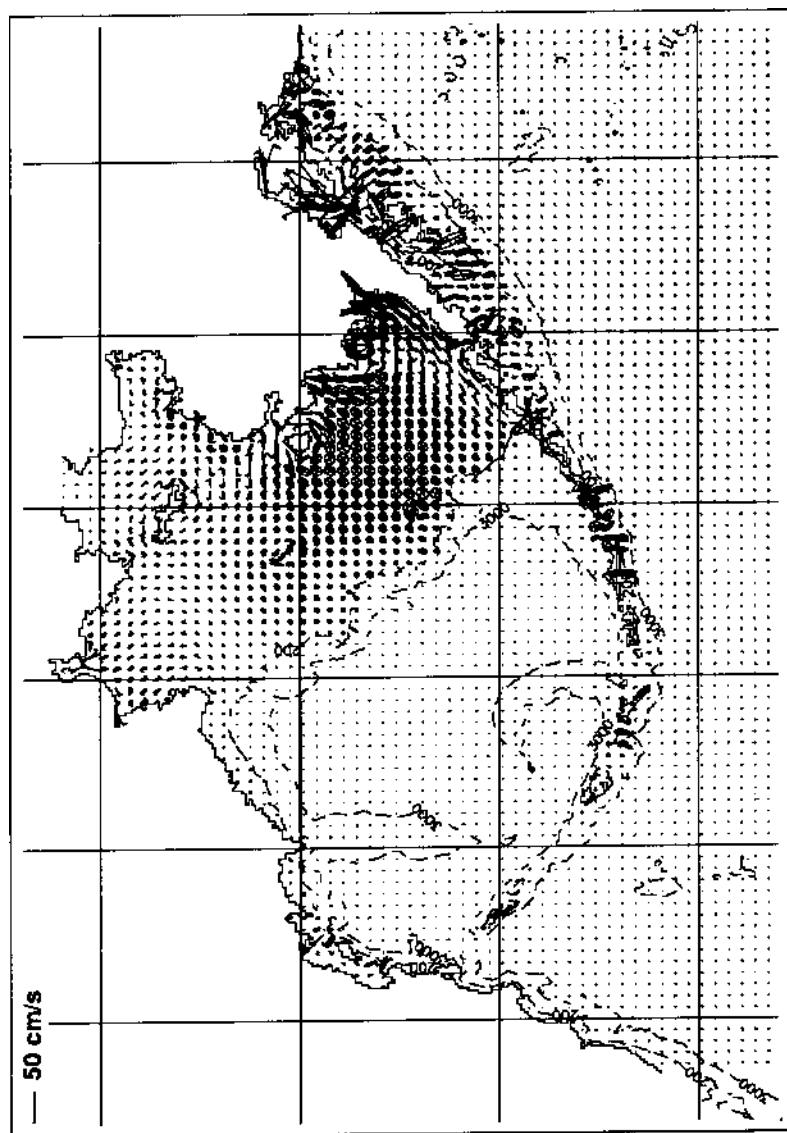


Figure 4. Tidal current ellipses for  $M_2$  wave in the Bering Sea.

data, but, because in Fig. 4 they are plotted in every fourth point of the numerical grid, it is difficult to follow the local velocity pattern. In the deep basin a velocity on the order of 1-2 cm/s occurs, while at the open shelf the velocity increases to 5-20 cm/s. The different velocity magnitude at the shelf and in the deep Bering Sea is obviously due to bathymetric enhancement of the tidal currents. Strong currents greater than 100 cm/s develop between Aleutian Islands due to narrow passages, and in Bristol Bay due to the elongated triangular shape of the bay. Also, high velocity on the order of 50 cm/s occurs close to the Pribilof Islands, St. Matthew Island, and in the strait dividing Nunivak Island from Alaska (Etolin Strait).

Distribution of co-amplitude and co-phase contours for the semidiurnal elliptical lunar constituent ( $N_2$ ) is depicted in Fig. 5. This constituent generally repeats both the large and small scale pattern of the  $M_2$  constituent with much smaller amplitudes. Again, the maximum of amplitude, about 70 cm, is located in Bristol Bay. The currents associated with this constituent (not shown) in the deep Bering Basin are very small. Over vast spaces of the shelf, currents are less than 5 cm/s. In shallow bays and in proximity to some islands they may reach 20 cm/s.

Distribution of co-amplitude and co-phase contours for the diurnal lunisolar declination constituent ( $K_1$ ) is given in Fig. 6. The amplitudes are in centimeters; phase angle is referred to Greenwich and is expressed in degrees. Over the vast regions of the deep basin neither phase angle nor amplitude of the  $K_1$  wave changes significantly. When impinging on a shelf slope region a diurnal tide develops maximum amplitude, approximately 40 cm high, with small local domes over canyons. An unusually broad local maximum of amplitude is located north of the Aleutian Islands between 170°W and 173°W (Amukta Pass). The largest amplitude, close to 90 cm, again occurs in the triangular Bristol Bay. As in a semidiurnal band of oscillations, the islands do modify a smooth run of isolines by introducing local perturbations. The calculated distribution of amplitudes and phases is similar to the distribution obtained by Kantha (1995) (the model's resolution was 22 km), and to the charts derived from satellite observations by Cartwright et al. (1991). Over shallow domains, models by Liu and Leendertse (1979, 1981, 1982, 1990) and measurements by Pearson et al. (1981) and Mofjeld (1986) agree well with the results depicted in Fig. 6.

In Fig. 7 the amplitude and phase for the  $O_1$  wave are given. The general pattern of this constituent is close to the pattern of the dominant diurnal wave  $K_1$ . Again, across the shelf break from the deep basin toward the shelf the distribution of amplitude depicts the maximum. North of Amukta Pass in the Aleutian Islands the local maximum of the  $O_1$  amplitude occurs in the region of  $K_1$  maximum. The largest amplitudes, close to 60 cm, are located at the head of Bristol Bay. To describe the distribution of currents in the diurnal band of oscillations the maximum current velocity has been depicted in Fig. 8. The upper panel shows the distribution for  $K_1$  tide, and the lower panel for  $O_1$ . The major constituent in the diurnal

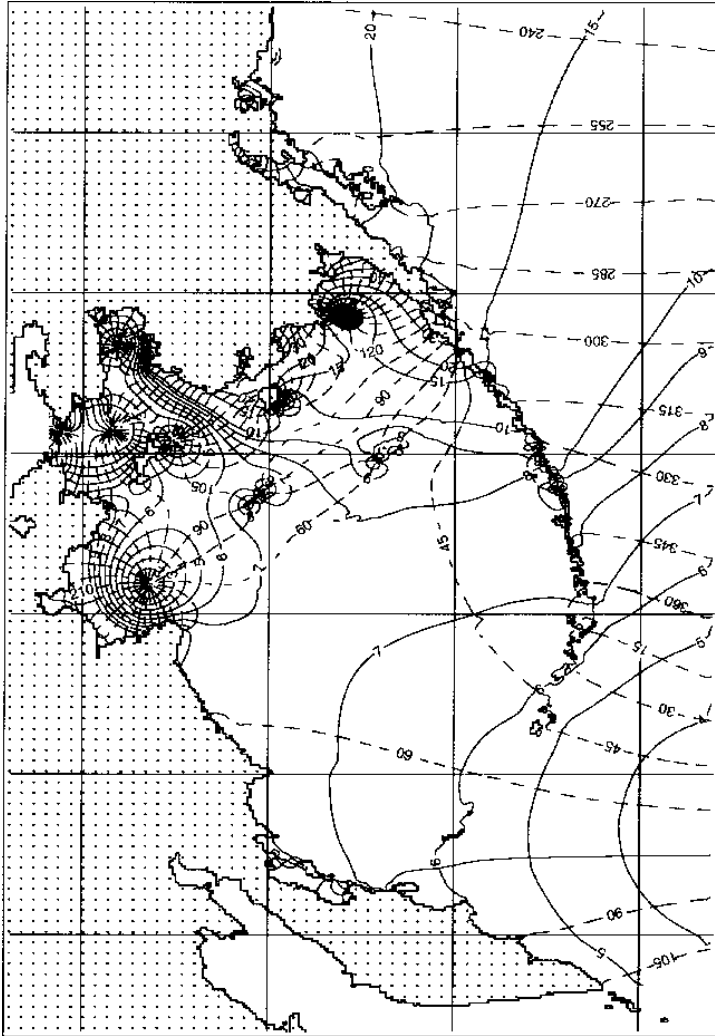


Figure 5. Computed amplitude (solid lines, in centimeters) and phase (dashed lines, in degrees) of surface elevation for the semidiurnal  $N_2$  tide, grid spacing = 9.26 km. The contours for the phase are plotted every 15°. Phase is referred to Greenwich.

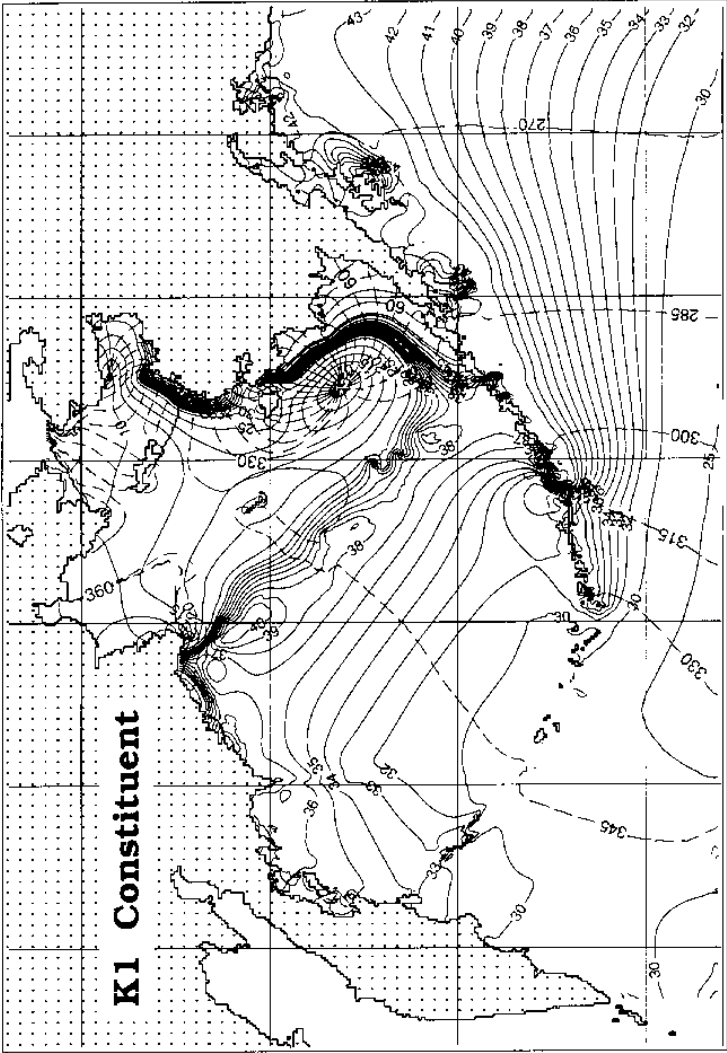
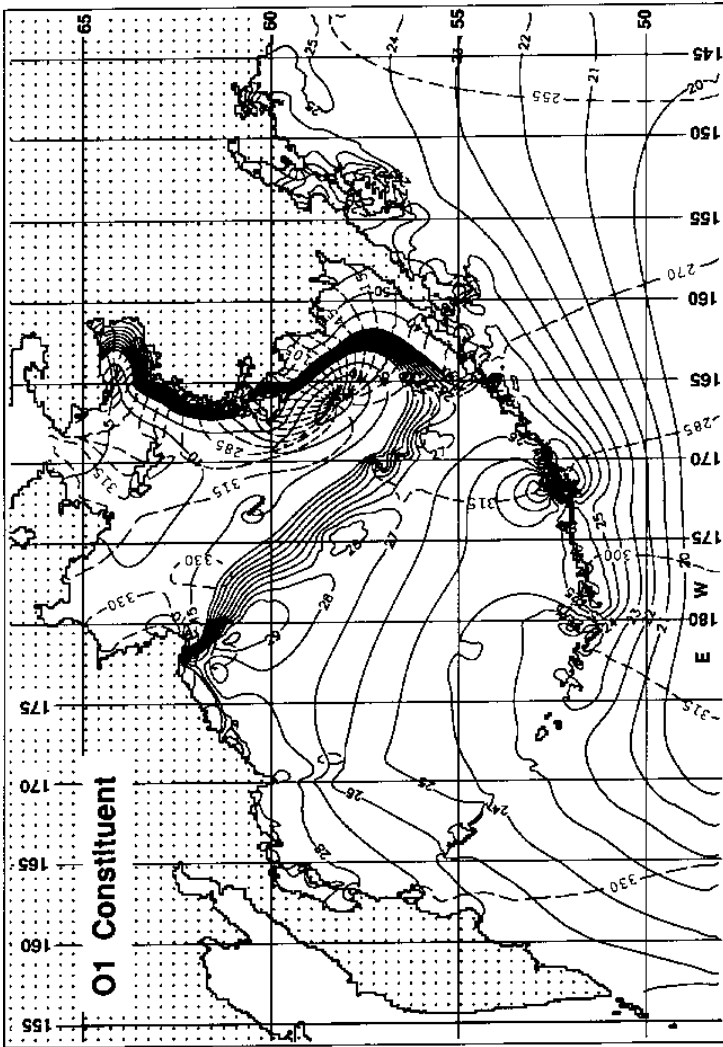


Figure 6. Computed amplitude (solid lines, in centimeters) and phase (dashed lines, in degrees) of surface elevation for the diurnal  $K_1$  tide, grid spacing = 9.26 km. The contours for the phase are plotted every 15°. Phase is referred to Greenwich.



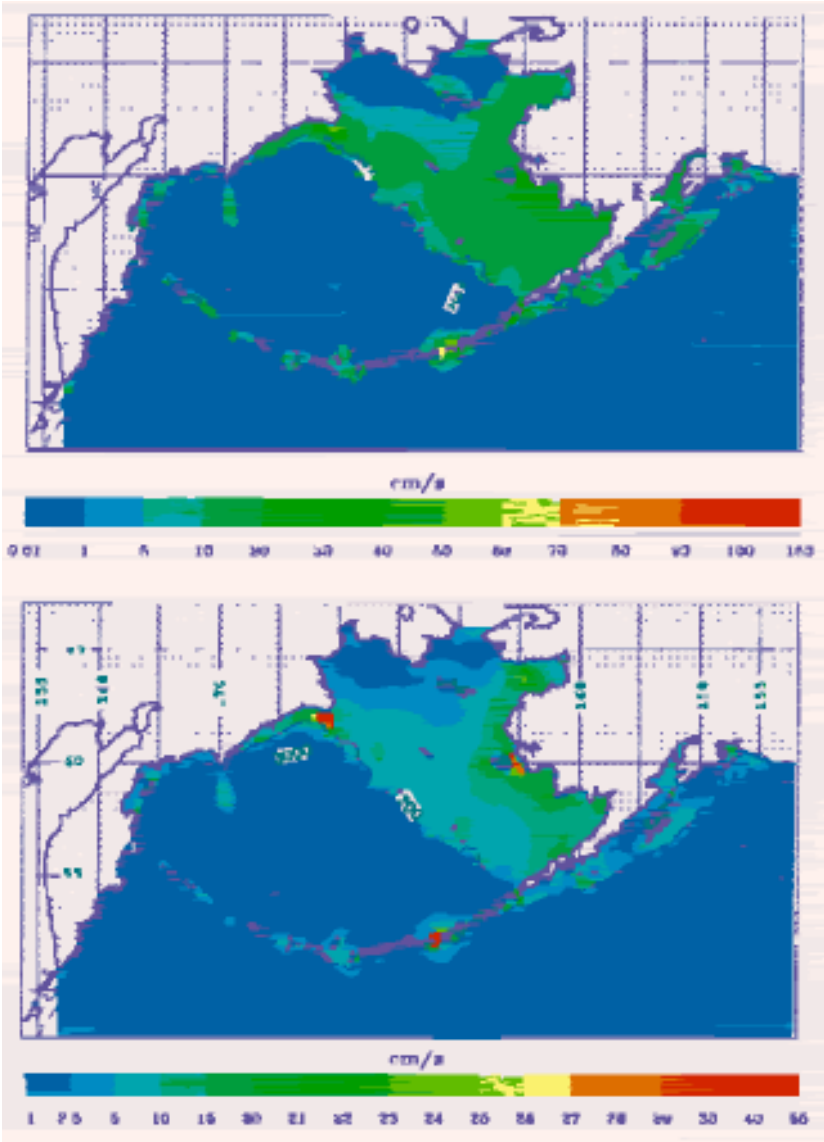


Figure 8. Maximum tidal currents, grid spacing = 9.26 km. Upper panel:  $K_1$  wave, lower panel:  $O_1$  wave.

band  $K_1$ , when compared against  $M_2$ , shows a stronger tendency for interaction with the bathymetry. Over the deep Bering Sea basin at the Shirshov Ridge, where the  $M_2$  tide generated currents close to 5 cm/s, the  $K_1$  current is enhanced up to 10 cm/s. The strongest currents on the order of 100 cm/s occur in Amukta Pass. Currents of about 50 cm/s are located south from Cape Navarin and in Etolin Strait. The maximum velocity for the  $O_1$  tide is shown in Fig. 8 lower panel. This constituent depicts even more strongly the three dominant regions of current amplification: off Cape Navarin, Amukta Pass, and Etolin Strait. The largest currents are close to 50 cm/s. The resolution of 9.26 km used for construction of the above charts for maximum velocity is too crude to show all local regions of enhancements in proximity to the islands and in the narrow straits.

In the ensuing discussion I will refer to  $M_2$  and  $K_1$  as representatives of semidiurnal and diurnal bands of tidal oscillations. Upon comparing the model results for the amplitude of the  $M_2$  (Fig. 3) and  $K_1$  (Fig. 6) waves, one striking difference was noticed in the region of the shelf break in both the Bering Sea and in the North Pacific south of the Aleutian Islands. The amplitude of the  $M_2$  wave at the shelf break region remains practically unchanged, whereas the amplitude of the  $K_1$  wave is enhanced over the same region. South of the Aleutian Islands the shelf is narrow so the amplification is less pronounced. In the Bering Sea the  $K_1$  wave exhibits maximum amplitude over the shelf break with many local maxima. Occurrence of the local maxima in proximity to the shelf break in the diurnal band of oscillations suggests the presence of trapped or partially trapped diurnal shelf waves (Kowalik and Proshutinsky 1993). The above charts, as well as data presented by Mofjeld (1986) and computations of Liu and Leendertse (1990) over the shelf domain, and Kantha's (1995) world tidal model, confirm existence of the maximum of the amplitude in the diurnal domain over the Bering Sea slope.

Velocity patterns of diurnal and semidiurnal waves are also quite different. While the velocity of  $M_2$  (Fig. 4) tends to be enhanced in shallow water and around islands, the velocity of  $K_1$  (Fig. 8, upper panel) in addition to the shallow water enhancement, is amplified at the shelf break depicting local maxima in proximity to the local maxima of sea level. Structures of enhanced tidal currents for the semidiurnal and diurnal constituents are often generated due to topographic amplification over shallow areas. An example of such amplification is shallow, triangular-shaped Bristol Bay (Figs. 4 and 8) and Etolin Strait. In the diurnal band of oscillations the maximum current is also associated with the shelf wave regions. Structures of enhanced tidal currents are generated by near-resonant shelf waves of tidal origin which are trapped, or partially trapped, over the bottom topography. Resonant transfer of energy from tidal wave to shelf wave occurs when the period of rotational mode of oscillation is close to the tidal period. Maximum velocity for  $K_1$ , as well as for  $O_1$  (Fig. 8), reveals two regions of enhanced currents in the Aleutian Islands and off Cape Navarin. These regions can also be identified in the sea level charts as locations

of the maxima in the sea level distribution. A number of smaller trapped waves can be identified along the Bering Sea shelf slope through the local maximum of the sea level (Fig. 6) and through the local maximum of the velocity (Fig. 8).

It is possible to delineate three modes of near-resonant interaction of diurnal tidal waves with bottom topography in the Bering Sea. The first mode exists in the Aleutian Islands region (Figs. 6 and 8) and most probably is caused by generation of resonance oscillation around islands (Longuet-Higgins 1969) or seamounts (Hunkins 1986, Chapman 1989, Haidvogel et al. 1993, Kowalik 1994). The second mode of oscillation occurs off Cape Navarin (Figs. 6 and 8) and is related to the abrupt changes in the shelf width along the coast. A shelf wave which enters such a domain is trapped or arrested and, if resonance conditions occur, local enhancement of the current follows (Kowalik and Proshutinsky 1993). The third mode of trapped oscillation occurs along the shelf break at the canyons. In ensuing investigations we shall study tides in the Pribilof Canyon, where measurements taken by Schumacher and Reed (1992) indicate strong diurnal currents. The horizontal scale of the trapped diurnal waves in the Bering Sea ranges from 20 km to 100 km. The tidal charts presented above are computed for the ice-free season. The pack ice usually covers the Bering Sea shelf with the ice boundary running along the shelf break from Cape Navarin to the Pribilof Islands. Along with the pack ice, some nearshore areas (especially in Norton Sound) are covered by shorefast ice. Mofjeld's (1986) investigations of the long series of currents and sea level data from the northeastern shelf of the Bering Sea shed some light on variation in the tidal harmonic constants. These variations are probably due to pack ice. One long series of sea level data from under the shorefast ice was analyzed by Johnson and Kowalik (1986). The physics of the ice-tide interaction is not well understood. The sea ice generally damps shorter wave oscillations in the water column which results in less turbulence and smaller vertical and horizontal eddy viscosity coefficients. Due to ice cover an additional drag force occurs (similar to the bottom drag) between ice and water. In addition, fast ice can change the geometry of the flow by changing depth or channel width. Canadian observation from Tuktoyaktuk revealed strong dependence of the tide on the ice cover (Murty 1985). The  $M_2$  constituent changed amplitude from 16 cm during summer to 11 cm during the winter. The nonlinear constituent  $M_4$  increased up to 100% during the winter. The observations on ice drift and deformation in the Bering Sea indicate possible strong nonlinear ice-water coupling in the tidal band of oscillations since the  $M_4$  tidal component of the ice velocity is relatively much stronger than the  $M_4$  in the ocean currents (Pease and Turet 1989). Data described by Mofjeld (1986) from the northwestern shelf show that the tidal harmonic constants change seasonally. The diurnal amplitude increased and semidiurnal amplitude decreased during winter. The increase and decrease amounted to a few percent of the mean values. The maximum change in amplitude is close to 3 cm and the maximum

change in phase is up to  $15^\circ$  for the  $M_2$  tide in the Bering Strait. The relatively high changes in amplitude (37% of the mean amplitude) at this site possibly express damping of the tides by the sea ice in the Arctic Ocean (Kowalik 1981).

Johnson and Kowalik (1986) analyzed a series of sea level data taken at Stebbins ( $\lambda = 162^\circ 20' \text{W}$ ,  $\phi = 63^\circ 30' \text{N}$ ), Norton Sound, in 1982, both under the fast ice and during summer. This region is dominated by diurnal tides ( $K_1$  amplitude is 47.4 cm during summer). The harmonic analysis showed that the amplitudes of the main constituents,  $K_1$ ,  $O_1$ , and  $M_2$ , increase from winter to summer by about 40%. The largest phase change ( $75^\circ$ ) occurred for the  $M_2$  constituent.

## Pribilof Islands and Canyon

The numerical lattice of 9.26 km, used for the whole Bering Sea, gives good resolution of the basic features of the tidal waves—including the identification of the major topographically trapped waves. A smaller scale is required for investigation of the tidal dynamics around islands, in the straits and at the shelf break, where interaction of the tide with the bottom slope changes tide dynamics. The region of the Pribilof Islands and Canyon (PIC) has been chosen for ensuing investigation because in this region the data are available for comparison against models. Generally, tides dominate the dynamics around the Pribilof Islands (Pearson et al. 1981). The interaction of tides and currents with bottom topography around islands, seamounts, and canyons often leads to current enhancement and, as a consequence, the nonlinear interactions become stronger in such regions (Haidvogel et al. 1993, Brink 1995). Enhanced tidal current causes stronger mixing along vertical directions; such mixing may erase vertical stratification and build a local tidal front. This process occurs in proximity to the Pribilof Islands. Both islands are surrounded by structure fronts that divide the well mixed inner shelf waters (0-40 m) from the two layers characteristic of the middle shelf (50-100 m). The tidal currents and the vertical mixing around islands can be important mechanisms in the transporting and concentration of nutrients, plankton, and zooplankton. Coyle et al. (1992) described such a mechanism through investigation of tidal currents around St. George Island and their effects on transport of zooplankton and adjustment of the feeding behavior of birds to the tidal cycle.

Satellite-tracked drifting buoys deployed on the Bering Sea southern shelf were advected northwestward to the vicinity of the Pribilof Islands (Kowalik and Stabeno, submitted; Stabeno et al., chapter 1, this volume). In this advective motion tidal loops are also evident. After reaching the Pribilof Islands, the buoys were trapped in a clockwise motion around the islands and then transported southward. A series of current meters deployed for several months around St. Paul Island revealed that the largest  $M_2$  tide currents (greater than 70 cm/s) occur at the southern tip of St. Paul Island, where total depth is close to 25 m (Kowalik and Stabeno, submitted;

Stabeno et al., chapter 1, this volume). This circulation pattern, which results in a trapped flow around the islands, can play an important role as a dynamic pathway for the transport and trapping of nutrients, plankton, and fish larvae in the vicinity of the Pribilof Islands. How this circulation traps foreign material near the islands can affect the productivity of these waters.

A high-resolution numerical grid with a space step of 1 nautical mile (1.852 km) in the region of PIC (Fig. 2) is used to study tidal motion around the islands and at the canyon. The results from the Bering Sea model serve as a boundary condition for the fine-scale model in the PIC domain (Fig. 2). The sea level calculated in the Bering Sea model is used to define elevations along the open boundaries of the PIC. The fine grid in the PIC domain is connected to the coarse grid through the linear interpolation of the coarse grid data.

A tide wave enters the Bering Sea as a progressive wave from the North Pacific through Aleutian Island passages (Pearson et al. 1981). The PIC domain is located both in the deep Bering Basin and at the shelf. Here the tides propagate from the deep basin into the shallow domain. Over the latter domain both amplitude and currents are strongly enhanced. To identify differences in semidiurnal and diurnal tidal waves, results of calculations for the  $M_2$  and  $K_1$  waves are considered. In Fig. 9, upper panel, amplitude of surface elevation for the  $M_2$  tide is given. Sea level amplitude slowly changes from 24 cm in the deep basin to 31 cm over the open shelf. An interesting pattern in the sea level occurs around the Pribilof Islands. The sea level depicts a dipole structure with minimum located at the southeastern shores and maximum at northern shores. Especially conspicuous is the 15 cm sea level change around St. Paul Island. (The rapid change of the sea level around this island refutes a general assumption that islands are good platforms for sea level measurements.)

Figure 9, lower panel, depicts the maximum of  $M_2$  tidal currents. The deep basin's sluggish flow on the order of 1 cm/s is enhanced over the shelf break to 5-10 cm/s. The isolines of the current magnitudes actually tend to repeat bathymetry contours. This is well depicted in Pribilof Canyon. Around the Pribilof Islands, due to topographic amplification and nonlinear interactions in the shallow water, currents up to 50-70 cm/s are generated. The driving mechanism which generates this trapped motion around the islands is a dipole structure of the sea level shown in Fig. 9, upper panel. The strength of the tidal stream will be proportional to the sea level difference in the dipole structure.

The tidal dynamics in the diurnal band of oscillations is illustrated through the major  $K_1$  constituent. Figure 10, upper panel, depicts a general pattern of slowly varying sea level from southwest to northeast with the maximum of amplitude, above 39 cm, along the shelf slope. A number of local sea level maxima can be discerned not only in the proximity of the islands but also along the shelf slope close to the 200 m depth contour. Especially pronounced is the maximum at the flank of the Pribilof Canyon.

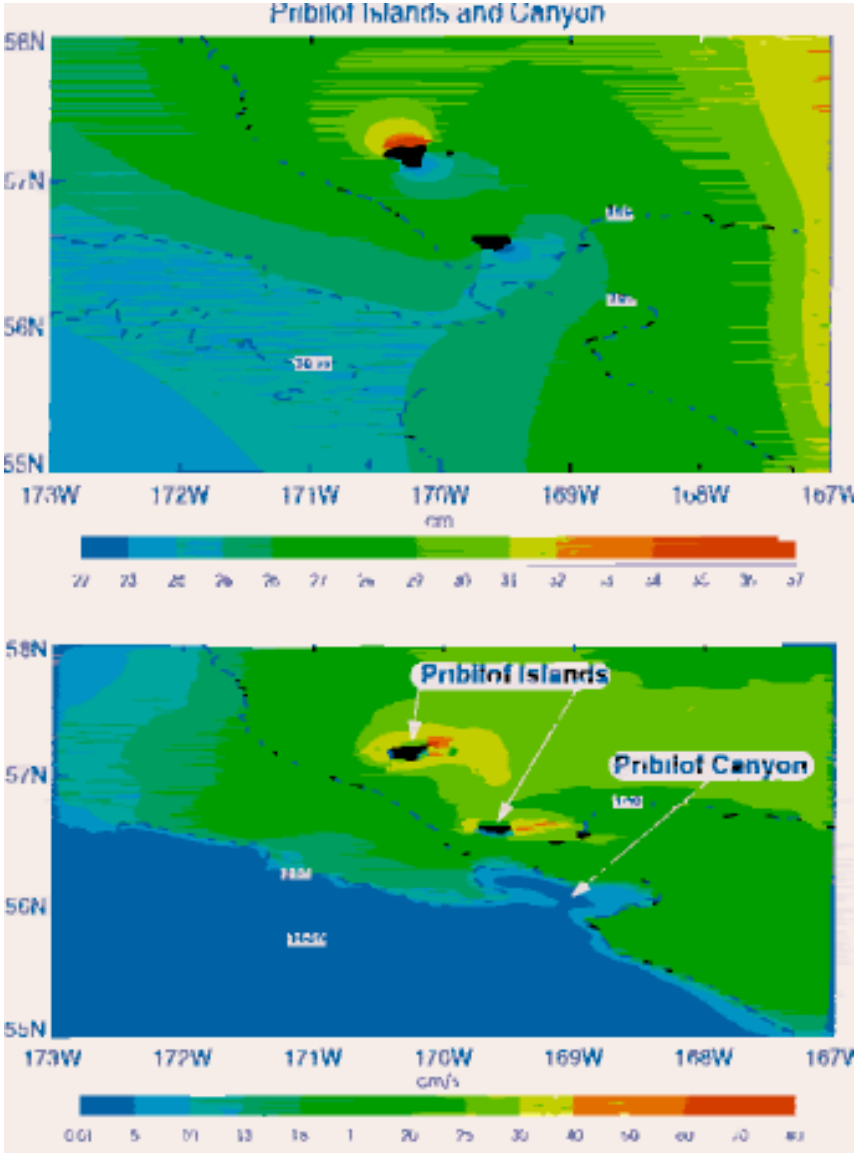


Figure 9. Pribilof Islands and Canyon. Space resolution 1.852 km. Dashed lines denote bathymetry in meters. Upper panel: computed amplitude of surface elevation for the semidiurnal  $M_2$  tide. Lower panel: maximum tidal currents of the  $M_2$  tide.

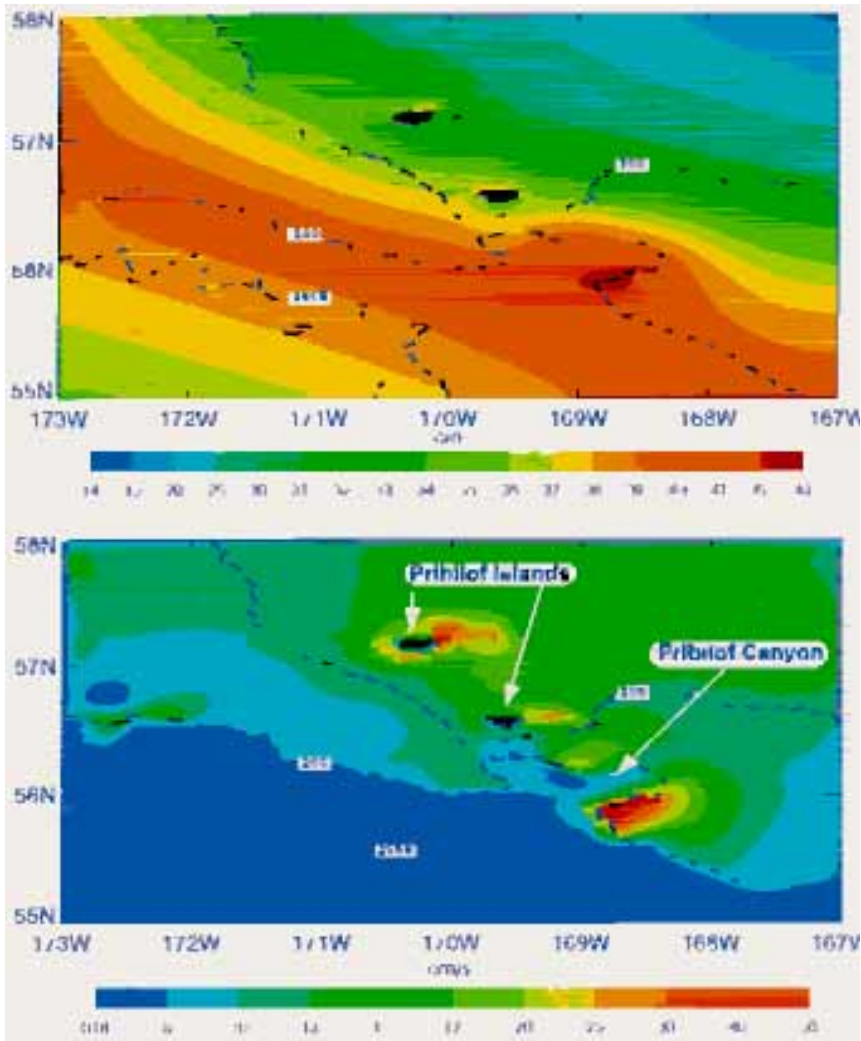


Figure 10. Pribilof Islands and Canyon. Space resolution 1.852 km. Dashed lines denote bathymetry in meters. Upper panel: computed amplitude of surface elevation for the diurnal  $K_1$  tide. Lower panel: maximum tidal currents of the  $K_1$  tide.

The  $K_1$  maximum currents are shown in Fig. 10, lower panel. Although in the large scale pattern one can see the enhancement of current from the deep basin to the shelf and enhancements in the shallow waters in the islands' proximity, the complete picture is more complicated than for the  $M_2$  tide. The enhancement of currents around islands is not the sole feature, because along the shelf slope in the domain of Pribilof Canyon, the new regions of the local enhancement have been generated. At the mid-slope location in Pribilof Canyon (272 m depth), long-term current meter records analyzed by Schumacher and Reed (1992) corroborate this local enhancement of the diurnal currents. The local regions of enhanced diurnal currents are related to the sea level distribution given in Fig. 10, upper panel. The size of the enhancement domain varies from about 20 km (Fig. 10, lower panel, northern flank of the Pribilof Canyon) to 50 km at the eastern flank of the canyon and to about 80 km at the Aleutian Islands (Fig. 8, upper panel).

The important conclusion is that the diurnal tide can generate enhanced currents not only in the shallow domains around islands but in the deeper domains in the shelf slope region as well. Again, this illustrates well the importance of the shelf waves in the cross-shelf exchange and suggests the possibility that along the shelf break north from the PIC region similar domains may exist.

The above computations were extended by Kowalik and Stabeno (submitted) into the local domain around St. Paul Island by application of a high-resolution 617 m numerical grid. The model data were used for comparison against current meter data. Several current meters were deployed in the vicinity of St. Paul Island from 13 September 1995 until 7 August 1996. The computed and observed currents were compared through the various ellipse parameters. The general pattern of the tidal motion deduced from measurements and model revealed that the largest tidal currents occurred at the southern tip of St. Paul Island, and that directions of the major axes of the tidal ellipses follow the equal bathymetry contours and are often parallel to the coastlines. The tidal current at the measuring site with the strongest flow ( $\lambda = 170^\circ 17.49' \text{W}$ ,  $\phi = 57^\circ 5.36' \text{N}$ ) showed the following values for the major axes of the tidal ellipse:  $M_2$ —71.6 cm/s,  $N_2$ —21.3 cm/s,  $K_1$ —19.8 cm/s,  $O_1$ —11.7 cm/s. The  $M_2$  tide dominates the tidal current field around the island. A glance at Figs. 9 and 10 reveals that the amplitude of diurnal and semidiurnal constituents is close to 30 cm. The difference is due to strength of the dipole in proximity to the island. The  $M_2$  tide shows much stronger variations in the sea level distribution around the island.

## Residual Tidal Currents

The nonlinear interactions of the tidal currents result in the new dynamics, which often differs from linear dynamics. The energy of the basic tidal constituents is transferred toward shorter and longer periods and

the tidal currents averaged over tidal period generate steady (residual) current. Observations on generation of the new periods are scarce, but those that are available do confirm importance of the fortnightly periodicity in the Bering Sea dynamics (Schumacher and Reed 1992). Application of the three-dimensional model to the nonlinear interaction of the tides by Liu and Leendertse (1990) suggests that the generation of the new periods is more effective above the bottom boundary layer.

Residual currents can be an important mechanism contributing to the mean flow. These currents are generated as a result of rectification process as the oscillating velocity interacts either with the sea surface or with the bottom topography. The interaction of tidal currents with bottom topography usually dominates the rectification process. In the process of generation of residual flow a significant role is played by advective terms in the equation of motion. Several attempts have been made to define residual circulation in the Bering Sea. Mofjeld et al. (1984) presented estimates of residual currents by fitting simple tidal waves to the observed tidal currents from two stations at the Bering Sea shelf. Estimated residual currents were smaller than 1 cm/s. Schumacher and Kinder (1983) arrived at similar residual velocity over the open Bering Sea shelf (far from islands and coastline). Liu and Leendertse (1990) demonstrated, through various shelf models, the importance of residual currents in Bering Sea circulation. In their model a resolution of about 20 km was used to investigate residual tidal currents of both barotropic and baroclinic origin. Close to the Bering Sea slope the model depicted residual currents from 2 to 5 cm/s. Recent long series of measurements by Staben (Kowalik and Staben submitted) in the shallow water around Pribilof Islands revealed mean residual tidal current on the order of 15 cm/s.

In numerical computation the residual velocities for the several constituents interacting together have been obtained by averaging an hourly time series over a period of 29 days. Even computations carried out with a numerical lattice of 9.26 km in the entire Bering Sea show quite developed residual motion. Most interesting is residual current along the Bering Sea shelf break. The local residual currents generated in proximity to the shelf break are interconnected, resulting in a single flow-through along the Bering Sea shelf slope from southeast to northwest. The average velocity of this current is less than 1 cm/s. This result suggests that some of the residual currents investigated by Liu and Leendertse (1990) are barotropically driven. Strong tidal currents, through nonlinear interactions, generate quite strong residual currents at two regions where the wide Bering Sea shelf changes into the narrow shelf (i.e., close to Cape Navarin and in proximity to the Aleutian Islands). Residual tidal currents in the Aleutian and Pribilof Islands regions are shown in Fig. 11, lower panel. The maximum residual current in the passages between the Aleutian Islands is about 15 cm/s. The mean flow should play an important role in exchange of properties between the north Pacific and the Bering Sea. Around numerous Aleutian islands and around the Pribilof Islands, residual currents

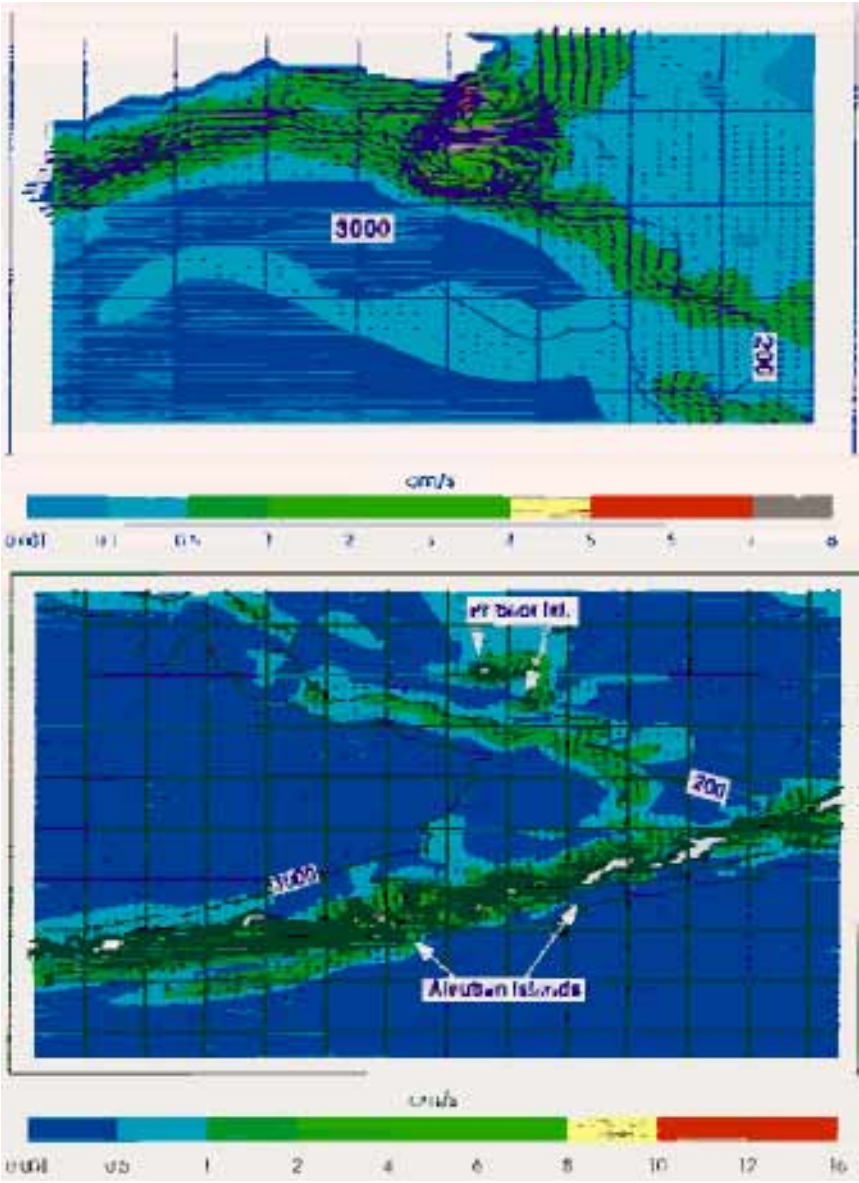


Figure 11. Residual tidal currents. Seven major constituents are considered, grid spacing = 9.26 km. Upper panel: off Cape Navarin. Lower panel: Aleutian Islands and Bering Sea slope.

render trapped clockwise circulation. In Amukta Pass such a circulation will result in an inflow to the Bering Sea on the eastern side of the pass and an outflow on the western side of the pass. This tidally driven circulation pattern agrees well with the general circulation pattern described in Amukta Pass by Reed and Stabeno (1997). Similar circulation was observed by Reed et al. (1993) in Near Strait and Amchitka Pass. Residual currents off Cape Navarin are given in Fig. 11, upper panel. A pair of eddies rotating in opposite directions, seen in this figure, is not confined to the shelf domain; this is probably an indication that these eddies play an important role in the exchange of properties between shelf and deep ocean.

Horizontal resolution of 9.26 km is too large to properly resolve all nonlinear interactions, but since the entire Bering Sea is being investigated the results quickly delineate major domains of interaction. A higher-resolution numerical grid with a space step of 1.852 km has been located in the PIC region to estimate residual flow both around the islands due to topographical enhancement of the tidal currents in the shallow water and at the canyon due to trapped shelf waves. Residual tidal motion calculated from a 9.26 km grid model for the whole Bering Sea depicts, in the shallow areas around the Pribilof Islands, quite a small velocity on the order of 1-2 cm/s. This small velocity exactly delineates the permanent clockwise eddy around the islands (see Fig. 11, lower panel). The mean currents depict about a 2.5-fold increase when grid spacing is diminished from 9.26 km to 1.852 km.

The horizontal resolution has been further increased around St. Paul Island to 617 m (see Fig. 2). This resolution is close to the grid distance recommended by Zimmerman (1978) for reproduction of the bottom topography with significant production of vorticity and nonlinearity. Calculations with this fine grid in the St. Paul subdomain confirm general clockwise circulation and the average and maximum residual velocities have grown considerably as can be seen in Fig. 12, upper panel. Maximum residual velocity has changed from approximately 10 cm/s in a 1.852 km grid up to 30 cm/s in a 617 m grid. In the island's vicinity the residual circulation is small and tends to be organized in local coastal eddies. At a distance of about 1-3 km from St. Paul Island the residual velocity attains greatest values and circles the island in continuous fashion. The average residual currents in this region are 10 to 15 cm/s, a considerable increase when this result is compared with 1-2 cm/s obtained in the 9.26 km grid. Additional results obtained for the  $M_2$  constituent computed alone without interaction with the remaining tidal constituents show that this constituent is primarily responsible for the generation of residual currents around St. Paul Island.

All current meters deployed in the vicinity of St. Paul Island during 1995-1997, except for site one, were deployed close to the 25 m isobath, 5 m above the bottom. At mooring site 1, two current meters were deployed in a water depth of 65 m. The residual flow around the island for the whole measuring period depicts stable clockwise flow in the range 4

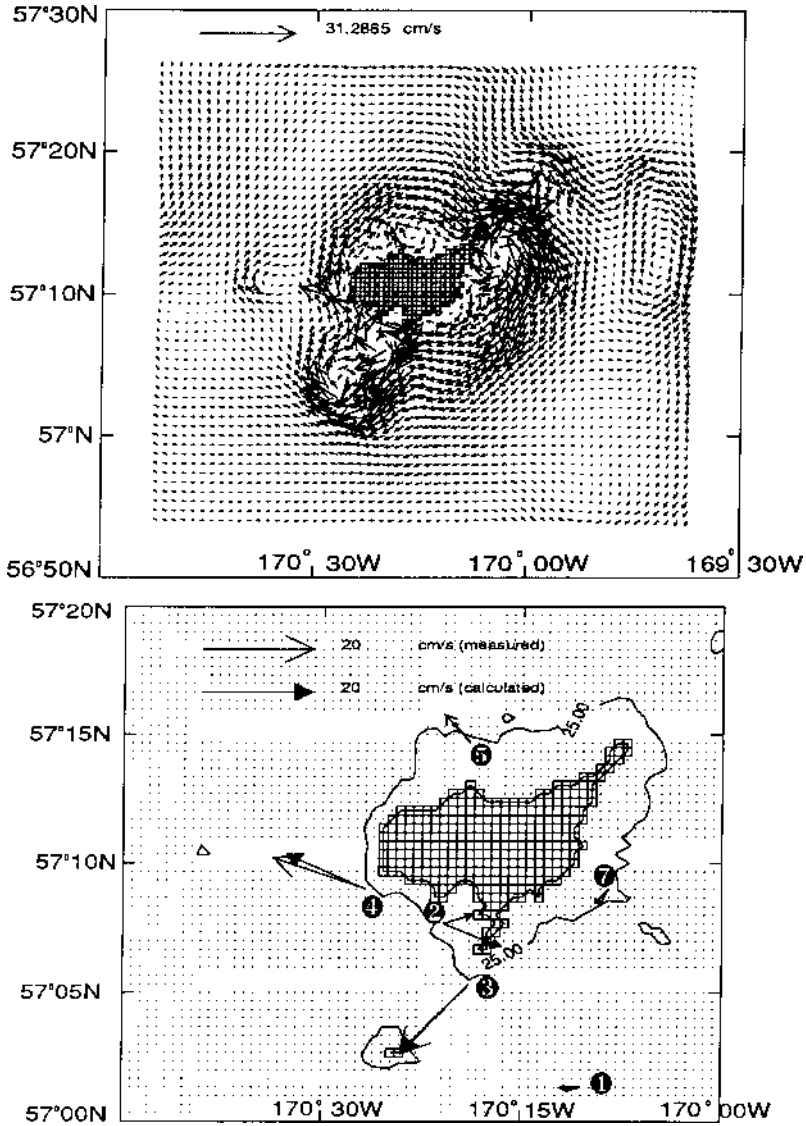


Figure 12. Residual tidal currents around St. Paul Island. Four major constituents are considered, grid spacing = 617 m. Upper panel: distribution derived from computation. Lower panel: measurements against model at the measuring sites.

to 18 cm/s. Stability in direction is quite amazing: flow reversal occurred only on 10 February. Circular currents around the island can be forced by density gradients or wind, but none of these mechanisms can depict stable behavior through the various seasons. The only permanent mechanism is rectifying the tidal currents to the low frequency currents.

A comparison of the measured residual currents with the currents obtained from the above computation is given in Fig. 12, lower panel. Computed current magnitude and direction turned out to be in good agreement with the current data obtained from the observations. The most interesting is current pattern in points 2 and 5. There, due to the local interaction with the bottom slope and coastline, the measured currents have been deflected from the general clockwise circulation. The local coastal eddies rendered through the fine resolution model (Fig. 12, upper panel) are responsible for this deflected flow pattern.

Phenomena of the tidally trapped motion and coastal eddies observed and measured around the Pribilof Islands probably occur in proximity to many islands in the Bering Sea. One confirmation of the tidally generated eddies is given by Ahlnas (1994) through satellite observations. The Synthetic Aperture Radar image showed multiple dipole eddies in the strait between St. Matthew Island (60°30'N, 172-173°W) and Hall Island. The eddies seem to be permanent features which concentrate nutrients, lead to considerable biological productivity, and sustain large bird populations in this area.

## **Model Versus Measurements**

The model results can be verified against various observations. Sea level observations are available from more than 50 stations in the Bering Sea, including a few from Russian coastal observations at Provideniya, Anadyr, Petropavlovsk, Port Siber, and Bering Island. The set of data obtained by Pearson et al. (1981), Mofjeld (1984, 1986) and Mofjeld et al. (1984) covers the Bering Sea shelf. An additional source of data is Geosat altimetry measurements (Cartwright et al. 1991). The satellite data are quite smooth but very close to the quality of the data set derived from a numerical model by Schwiderski with resolution of 1° (R.D. Ray, NASA Goddard Space Flight Center, pers. comm., January 1998).

Current meter data from more than 30 locations are available. These data were acquired through the efforts of Pearson et al. (1981), Mofjeld (1986), Schumacher and Reed (1992), and Kowalik and Staben (submitted).

In a series of papers related to the Bering Sea shelf Mofjeld (1984, 1986) reported tidal harmonics for sea level and currents, together with comparisons with numerical models. The computed elevations were in satisfactory agreement with those obtained from observations. Especially good similarity was obtained by Liu and Leendertse (1979, 1990) through application of three-dimensional models. When these models were driven

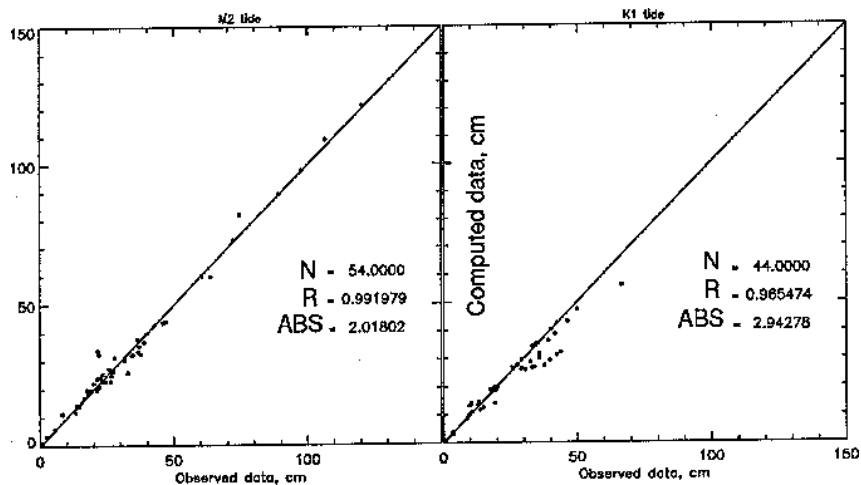


Figure 13. Computed versus observed sea level elevations in the Bering Sea, for the  $M_2$  (left) and for the  $K_1$  (right).  $N$  denotes number of stations,  $R$  coefficient of correlation,  $ABS$  absolute error between observed and calculated elevation in centimeters.

with the sea level forcing due to tides, the computed currents agreed well with the observed currents.

Here I extend the comparison between model and measurements to sea level over the entire Bering Sea domain. The comparison between measured and computed sea level for the  $M_2$  and  $K_1$  constituents is given in Fig. 13. A high correlation coefficient shows satisfactory agreement between measured and computed sea level. The few points with higher deviation from the line are attributed to the measurements taken in the river mouth and narrow bays where model resolution is inadequate for the reproduction of bathymetry and coastline. The general tidal charts obtained through computations are in satisfactory agreement with satellite-derived sea level. Enhancement of the diurnal sea level over the shelf break in the Bering Sea is especially well depicted.

For comparison of the computed versus measured tidal currents a data set from the shallow part of the Bering Sea is available. These data were thoroughly analyzed and compared with numerical models by Pearson et al. (1981), Mofjeld (1984, 1986), and Kowalik and Stabeno (submitted). A set of data for the Pribilof Canyon region has been acquired by Schumacher and Reed (1992). Here I limit my comparison to the data available in the region of the Pribilof Islands and Canyon where we applied a high resolution barotropic model (Figs. 9, 10). Data from six stations in the region are available for comparison against the model. Basic param-

**Table 1. Comparison of measured and computed tidal ellipse parameters.**

Station	Total depth	Depth of current meter	Long	Lat	$K_1$				$M_2$			
					Major		Minor		Major		Minor	
					H	D	H	R	H	D	H	R
BC17	104	96	56 34	167 34	9.1	105	4.3	C	15.9	53	10.5	C
Calc					9.8	119	5.4	C	17.1	47	11.1	C
BBL2	69	64	57 37	167 45	11.7	296	4.5	C	21.3	42	16.6	C
Calc					12.6	305	4.6	C	20.1	48	16.2	C
BP1	140	50	56 16	169 48	8.5	176	3.4	C	9.0	43	6.5	C
BP1	140	125	56 16	169 48	15.7	168	2.9	C	12.0	108	9.3	C
Calc					8.5	138	5.6	C	9.2	59	6.0	C
BP2	287	62	56 14	169 42	4.6	167	1.1	C	12.7	36	10.6	C
BP2	287	137	56 14	169 42	10.8	155	5.8	C	9.8	10	5.8	C
BP2	287	272	56 14	169 42	19.8	137	4.7	C	6.5	122	4.5	C
Calc					5.1	107	1.6	C	7.9	54	5.1	C
BP2A	275	49	56 10	168 53	7.9	269	3.5	C	19.1	29	13.9	C
BP2A	275	124	56 10	168 53	6.8	272	2.6	C	11.1	52	7.1	C
BP2A	275	260	56 10	168 53	6.7	253	4.1	C	10.5	107	9.1	C
Calc					8.2	245	3.8	C	12.5	42	8.4	C
BP3	1,002	52	56 07	169 16	4.6	240	1.7	C	5.6	354	3.1	C
BP3	1,002	127	56 07	169 16	3.4	211	0.6	C	7.6	351	5.9	C
BP3	1,002	262	56 07	169 16	2.3	287	2.0	C	12.2	16	10.4	C
BP3	1,002	502	56 07	169 16	7.7	299	0.5	C	7.5	312	5.9	C
Calc					4.3	260	1.5	C	6.4	59	4.0	C

Depth is in meters, amplitudes H are in cm/s, D is direction of the major axis in degrees from the North, R refers to direction of rotation, and C denotes clockwise rotation.

ters of tidal ellipse, measured and calculated, are given in Table 1. Two relatively shallow water stations, BC17 (examined by Pearson et al. 1981) located east from Pribilof Canyon and BBL2 (examined by Mofjeld et al. 1984) located northeast from Pribilof Islands, show typical tidal velocities away from the shelf break. The computed tidal velocities are in satisfactory agreement with those obtained from the observations. Data from stations denoted as BP were collected by Schumacher and Reed (1992) at both the shelf break of the north-northwest side of Pribilof Canyon and the deep portion. Data at three stations show that the tidal current magnitude changes along the vertical direction, indicating that these tides are of baroclinic nature. The calculated tidal currents fall in the range of the lowest observed values along the vertical direction. In this geographical region the model predicts only slight enhancement of the diurnal tidal currents (Fig. 10). It is useful to note that at the three stations with baroclinic behavior the  $K_1$  velocity increases toward the bottom. This pattern is consistent with baroclinic diurnal trapped waves described through

models by Brink (1995) and Haidvogel et al. (1993) and through measurements by Eriksen (1991). The second set of data, which partly identifies the diurnal shelf waves at the shelf break, is a time series taken by Kitani and Kawasaki (1979). Two important conclusions can be drawn from their results. In all observations the ratio of the diurnal to semidiurnal tidal currents changes with depth and is much higher in the bottom layer than in the surface layer, thus confirming the general pattern observed in the trapped baroclinic waves. At two stations (St. 20 located at 60°N, 178°20'W and St. 61 located at 58°30'N, 173°15'W) diurnal currents dominate over semidiurnal currents in both the surface and bottom boundary layers. These two stations are situated close to the local maxima of velocity rendered in Fig. 8, upper panel.

It is difficult to find suitable measurements to confirm the general circulation pattern related to residual tidal currents along the Bering Sea slope. Fortunately, recent measurements in proximity to the Pribilof Islands confirm clockwise residual currents generated through the nonlinear interactions with quite high mean motion on the order of 15 cm/s (Kowalik and Stabeno, submitted). These observations compare well with the model simulations (Fig. 12).

## Summary and Discussion

A tidal model with a resolution of about 10 km in the Bering Sea and submodels with resolution of 1.852 km and 0.617 km in the Pribilof Islands and Canyon have been constructed. The numerical solutions thus obtained are depicted through corange, cotidal, and tidal current charts. These numerical solutions together with all available information either from measurements or from models have been investigated. I focus especially on tidal currents and on origin and location of enhanced tidal currents. The high resolution used in computations allowed me to define details which were not attainable in previous computations and measurements. The numerical approach delineated regions of large tidal currents in the Bering Sea. Generally, computations confirmed enhancement of the tidal currents at the shallow water in bays and around islands as described by Mofjeld (1986), Liu and Leendertse (1990), and Kowalik and Stabeno (submitted). A more complicated picture is associated with the diurnal constituent along the shelf break. A homogeneous "classical" long wave tidal pattern along the continental slope is often broken by a smaller scale pattern related to trapped shelf waves of tidal origin. These regions require both special measuring and modeling approaches, because over a relatively short distance, the sea level and the currents vary considerably. In the Bering Sea two regions of enhanced diurnal tidal currents are found: in the Aleutian Islands (Amukta Pass) and off Cape Navarin. A number of smaller regions have been identified along the Bering Sea shelf break.

Do measurements provide a suitable test for shelf waves of tidal origin? Analysis of data by Mofjeld (1986) and three-dimensional models by

Liu and Leendertse (1990) shows clearly the maximum of the sea level in the diurnal band along the Bering Sea shelf break, and a decrease in amplitudes with distance shoreward. The same maximum is well depicted in the satellite data of Cartwright et al. (1991) and in Kantha (1995), as well as in the present model.

Only two sets of current observations point toward occurrence of the diurnal shelf waves. A time series taken by Kitani and Kawasaki (1979) shows enhanced diurnal tidal currents along the shelf break, and a time series obtained by Schumacher and Reed (1992) shows enhanced diurnal waves in the Pribilof Canyon. Future searches for new regions of enhanced currents should be facilitated by identification of the general regions of diurnal trapped waves made through the models and measurements.

Enhanced currents, through advective terms and bottom friction lead to stronger nonlinear interactions resulting in the new periodical oscillations and residual circulation. Mean residual flow can be a major driving mechanism for circulation around islands and in the passages between the Aleutian Islands. The presence of the strong oscillating and residual tidal currents in the Aleutian passages will certainly have a bearing on how tidal effects are to be incorporated into mechanisms that contribute to exchange of properties between the North Pacific and the Bering Sea. The homogenization of water properties in Amukta and Amchitka passes is believed to result from tidal motion (Reed et al. 1993, Reed and Stabenro 1994).

The occurrence of the enhanced currents in local regions along the shelf break should also modify our notion on the exchange mechanism between shelf and deep oceanic waters. Maximum production in the shallow northwest Bering Sea occurs, according to Springer and McRoy (1993), in pools of especially prolific growth. The investigations carried out during ISHTAR (Coachman and Hansell 1993) suggest an advective supply of nutrients to these pools via a north-flowing current that originates along the continental slope and bifurcates at Cape Navarin. This is a source region and the pathway for elevated primary production throughout spring, summer, and fall (Iverson et al. 1979). At present the pathways for the nutrients and phytoplankton in this region are not clear. Computations off Cape Navarin show strong tidal currents not only at the shelf but at the shelf break as well. This suggests the possibility of tidal pumping of nutrients from the deeper water to the shelf domain and subsequent transport of nutrients and plankton by residual tidal currents into the Gulf of Anadyr.

## **Acknowledgments**

I would like to express my gratitude to L.H. Kantha from the University of Colorado, Boulder, for discussion of tides in the Pacific and for offering boundary data for the Bering Sea model; to A.Yu. Proshutinsky from the Institute of Marine Science, University of Alaska Fairbanks, for his help throughout the work; to R.D. Ray from NASA Goddard Space Flight Center

for offering Geosat altimetry data and discussions; and to P. Stabeno from NOAA/PMEL for sharing her knowledge and data on tides around Pribilof Islands. I am grateful to J.D. Schumacher (Twocrow) from NOAA/PMEL and anonymous reviewers for comments and improvements that strengthened this paper. Support from the Office of Naval Research under grant N00014-95-1-0929 and from Cooperative Institute for Arctic Research, University of Alaska Fairbanks, is gratefully acknowledged.

## References

- Ahlnas, K. 1994. Tidally generated dipole eddies around St. Matthew Island, Bering Sea. In: T. Vihma (ed.), Report series in geophysics. University of Helsinki, Department of Geophysics. 28:11-17.
- Bogdanov, K.T., V.V. Gorbachev, and V.V. Morozov. 1991. Atlas of tides of the Bering, Okhotsk and Japan seas. Okieanologicheskii Institute Akademi Nauk SSSR, Vladivostok. 39 pp.
- Brink, K.H. 1995. Tidal and lower frequency currents above Fieberling Guyot. *Journal Geophysical Research* 100:10817-10832.
- Cartwright, D.E., R.D. Ray, and B.V. Sanchez. 1991. Oceanic tide maps and spherical harmonic coefficients from Geosat altimetry. NASA Technical Memorandum 104544. 75 pp.
- Chapman, D.C. 1989. Enhanced subinertial diurnal tides over isolated topographic features. *Deep-Sea Research* 36:815-824.
- Coachman, L.K., and D.A. Hansell (eds.). 1993. ISHTAR: Inner shelf transfer and recycling in the Bering and Chukchi seas. *Continental Shelf Research* 13:473-704.
- Coyle, K.O., G.L. Hunt Jr., M.B. Decker, and T.J. Weingartner. 1992. Murre foraging, epibenthic sound scattering and tidal advection over a shoal near St. George Island, Bering Sea. *Marine Ecology Program Series* 83:1-14.
- Eriksen, C.C. 1991. Observations of amplified flows atop a large seamount. *Journal Geophysical Research* 96:15227-15236.
- Foreman, M.G.G. 1978. Manual for tidal current analysis and prediction. Institute of Ocean Sciences, Pacific Marine Science Report 78-6. 70 pp.
- Gill, A.E. 1982. Atmosphere-ocean dynamics. Academic Press, New York. 662 pp.
- Haidvogel, D.B., A. Beckmann, D.C. Chapman, and R.-Q. Lin. 1993. Numerical simulation of flow around tall isolated seamount. Part II: Resonant generation of trapped waves. *Journal Physical Oceanography* 23:2373-2391.
- Hastings, J.R. 1976. A single-layer hydrodynamical-numerical model of the eastern Bering Sea shelf. *Marine Science Communication* 2:335-356.
- Hendershott, M.C. 1977. Numerical models of ocean tides. In: *The sea*, vol. 6. John Wiley & Sons, New York, pp. 47-96.

- Hunkins, K. 1986. Anomalous diurnal tidal currents on the Yermak Plateau. *Journal Marine Research* 44:51-69.
- Iverson, R.L., L.K. Coachman, R.T. Cooney, T.S. English, J.J. Goering, J.L.J. Hunt, M.C. Macaulay, C.P. McRoy, W.S. Reeburg, and T.E. Whitledge. 1979. Ecological significance of fronts in the southeastern Bering Sea. In: R.J. Livingston (ed.), *Ecological processes in coastal and marine systems*. Plenum Press, New York, pp. 437-466.
- Johnson, W.R., and Z. Kowalik. 1986. Modeling of storm surges in the Bering Sea and Norton Sound. *Journal Geophysical Research* 91:5119-5128.
- Kantha, L.H. 1995. Barotropic tides in the global oceans from a nonlinear tidal model assimilating altimetric tides. 1. Model description and results. *Journal Geophysical Research* 100:25283-25308.
- Kinder, T.H., and J.D. Schumacher. 1981. Circulation over the continental shelf of the southeastern Bering Sea. In: D.W. Hood and J.A. Calder (eds.), *The eastern Bering Sea Shelf: Oceanography and resources*, vol. 1, pp. 53-76. Published by the Office of Marine Pollution Assessment, NOAA and BLM. Distributed by the University of Washington Press, Seattle, WA 98105.
- Kitani, K., and S. Kawasaki. 1979. Oceanographic structure on the shelf edge region of the eastern Bering Sea: I. The movement and physical characteristics of water in summer, 1978. *Bulletin Far Seas Fisheries Research Laboratory* 17:1-12.
- Kowalik, Z. 1981. A study of the  $M_2$  tide in the ice-covered Arctic Ocean. *Modeling, Identification, Control* 2:201-223.
- Kowalik, Z. 1994. Modeling of topographically-amplified diurnal tides in the Nordic Seas. *Journal Physical Oceanography* 24(8):1717-1731.
- Kowalik, Z., and A.Y. Proshutinsky. 1993. Diurnal tides in the Arctic Ocean. *Journal Geophysical Research* 98:16449-16468.
- Kowalik, Z., and P. Stabenho. Submitted. Trapped motion around the Pribilof Islands in the Bering Sea. *Journal Geophysical Research*.
- LeProvost, C., M.L. Genco, and F. Lyard. 1994. Spectroscopy of the world ocean tides from a finite element hydrodynamic model. *Journal Geophysical Research* 99:24,777-24,797.
- Liu, S.K., and J.J. Leendertse. 1979. Three-dimensional model for estuaries and coastal seas: VI: Bristol Bay simulations. The RAND Corp. R-2405-NOAA.
- Liu, S.K., and J.J. Leendertse. 1981. A three-dimensional model of Norton Sound under ice cover. In: *Proceedings of the Sixth International Conference Port. and Ocean Engineering under Arctic Conditions*. POAC, Quebec, Canada, pp. 433-443.
- Liu, S.K., and J.J. Leendertse. 1982. Three-dimensional model of Bering and Chukchi Sea. *Coastal Engineering* 18:598-616.
- Liu, S.K., and J.J. Leendertse. 1990. Modeling of the Alaskan continental shelf waters. *OCSEAP Final Reports* 70:123-275.

- Longuet-Higgins, M.S. 1969. On the trapping of long-period waves around islands. *Journal Fluid Mechanics* 37:773-784.
- Mofjeld, H.O. 1984. Recent observations of tides and tidal currents from the north-eastern Bering Sea shelf. NOAA Technical Memo ERL PMEL-57. 36 pp.
- Mofjeld, H.O. 1986. Observed tides on the northeastern Bering Sea shelf. *Journal Geophysical Research* 91:2593-2606.
- Mofjeld, H.O., J.D. Schumacher, and D.J. Pashinski. 1984. Theoretical and observed profiles of tidal currents at two sites of the southeastern Bering Sea shelf. NOAA Technical Memo ERL PMEL-62. 60 pp.
- Murty, T.S. 1985. Modification of hydrographic characteristics, tides, and normal modes by ice cover. *Marine Geodesy* 9(4):451-468.
- Pease, C.H., and P. Turet. 1989. Sea ice drift and deformation in the western Arctic. *EEE Publ. N. 89CH2780/5*, pp. 1276-1281.
- Pearson, C.A., H.O. Mofjeld, and R.B. Tripp. 1981. Tides of the eastern Bering Sea shelf. In: D.W. Hood and J.A. Calder (eds.), *The eastern Bering Sea Shelf: Oceanography and resources*, University of Washington Press, Seattle, pp. 111-130.
- Ray, R.D., and B.V. Sanchez. 1989. Radial deformation of the earth by oceanic tide loading. NASA Technical Memo 100743. 51 pp.
- Reed, R.K., G.V. Khen, P.J. Stabeno, and A.V. Verkhunov. 1993. Water properties and flow over the deep Bering Sea basin, summer 1991. *Deep-Sea Research* 40(11/12):2325-2334.
- Reed, R.K., and P.J. Stabeno. 1994. Flow along and across the Aleutian Ridge. *Journal Marine Research* 52:639-648.
- Reed, R.K., and P.J. Stabeno. 1997. Long-term measurements of flow near the Aleutian Islands. *Journal Marine Research* 55:565-575.
- Robinson, I.S. 1981. Tidal vorticity and residual circulation. *Deep-Sea Research, Part A* 28:195-212.
- Schumacher, J.D., and T.H. Kinder. 1983. Low-frequency current regimes over the Bering Sea shelf. *Journal Physical Oceanography* 13:607-623.
- Schumacher, J.D., and R.K. Reed. 1992. Characteristics of current over the continental slope of the eastern Bering Sea. *Journal Geophysical Research* 97:9423-9433.
- Schumacher, J.D., and P.J. Stabeno. 1998. The continental shelf of the Bering Sea. In: A.R. Robinson and K.H. Brink (eds.), *The sea: The global coastal ocean regional studies and synthesis*, Vol. XI. John Wiley and Sons, New York, pp. 869-909.
- Schwiderski, E.W. 1979. Global ocean tides, Part II: The semidiurnal principal lunar tide ( $M_2$ ). *Atlas of tidal charts and maps*. Naval Surface Weapon Center, Dahlgren, VA 22248. 87 pp.
- Schwiderski, E.W. 1981a. Global ocean tides, Part III: The semidiurnal principal solar tide ( $S_2$ ). *Atlas of tidal charts and maps*. Naval Surface Weapon Center, Dahlgren, VA 22248. 96 pp.

- Schwiderski, E.W. 1981b. Global ocean tides, Part IV: The diurnal lunisolar declination tide ( $K_1$ ). Naval Surface Weapon Center, Dahlgren, VA 22248. 87 pp.
- Schwiderski, E.W. 1981c. Global ocean tides, Part V: The diurnal principal lunar tide ( $O_1$ ). Naval Surface Weapon Center, Dahlgren, VA 22248. 85 pp.
- Schwiderski, E.W. 1981d. Global ocean tides, Part VI: The semidiurnal elliptical lunar tide ( $N_2$ ). Naval Surface Weapon Center, Dahlgren, VA 22248. 86 pp.
- Schwiderski, E.W. 1981e. Global ocean tides, Part VII: The diurnal principal solar tide ( $P_1$ ). Naval Surface Weapon Center, Dahlgren, VA 22248. 86 pp.
- Schwiderski, E.W. 1981f. Global ocean tides, Part IX: The diurnal elliptical lunar tide ( $Q_1$ ). Naval Surface Weapon Center, Dahlgren, VA 22248. 86 pp.
- Springer, A.M., and C.P. McRoy. 1993. The paradox of pelagic food webs in the northern Bering Sea—III. Patterns of primary production. *Continental Shelf Research* 13:575-599.
- Sunderman, J. 1977. The semidiurnal principal lunar tide  $M_2$  in the Bering Sea. *Deutsche Hydrographie Zeitschrift* 30:91-101.
- Yanagi, T., M. Shimizu, T. Saino, and T. Ishimaru. 1992. Tidal pump at the shelf edge. *Journal Oceanography* 48:13-21.
- Zimmerman, J.T.F. 1978. Topographic generation of residual circulation by oscillatory (tidal) currents. *Geophysical Astrophysical Fluid Dynamics* 11:35-47.

